
A Dynamic Network Simulator for Immiscible Two-Phase Flow in Porous Media

Santanu Sinha · Magnus Aa. Gjennestad · Morten Vassvik · Alex Hansen

Received: date / Accepted: date

Abstract We present in detail a set of algorithms to carry out fluid displacements in a dynamic pore-network model of immiscible two-phase flow in porous media. The algorithms are general and applicable to regular and irregular pore networks in two and three dimensions with different boundary conditions. Implementing these sets of algorithms, we describe a dynamic pore-network model and reproduce some of the fundamental properties of both the transient and steady-state two-phase flow. During drainage displacements, we show that the model can reproduce the flow patterns corresponding to viscous fingering, capillary fingering and stable displacement by altering the capillary number and the viscosity ratio. In steady-state flow, the model verifies the linear to non-linear transition of the effective rheological properties and satisfy the relations between the seepage velocities of two-phase flow in porous media.

1 Introduction

Flow of multiple immiscible fluids inside a porous medium shows a range of complex characteristics during transient as well as in steady state [1, 2]. A number of factors, such as the capillary forces at the interfaces, viscosity contrast between the fluids, wettability and geometry of the system, make the multiphase flow properties very different compared to single phase flow. When a non-wetting fluid displaces a wetting fluid the flow is called as drainage whereas the opposite is called imbibition. During drainage, a less-viscous fluid displacing a more-viscous fluid in a porous medium creates a variety of fingering patterns, whereas a more viscous fluid displacing a less-viscous one shows a stable displacement front [3, 4]. The fingering patterns show different properties depending on whether the flow is dominated by capillary or viscous forces and correspondingly they are named as the capillary and viscous fingerings respectively [5, 6]. The capillary fingering patterns appear during slow displacement process and are well described by invasion percolation [7, 8], whereas the viscous fingering patterns appear during fast displacement and can be modeled by diffusion limited aggregation (DLA) model [9, 10]. If both the fluids are continuously fed into the porous medium, the initial transients will eventually die out and the system enters a steady state. It has been discovered that under steady-state conditions, the two-phase flow rate do not obey the linear Darcy law in the capillary dominated regime. Rather, it was found to have a power law dependence on the total pressure drop [11–15].

Santanu Sinha
Beijing Computational Science Research Center, 10 East Xibeiwang Road, Haidian District, Beijing 100193, China.
E-mail: santanu@csrc.ac.cn

Magnus Aa Gjennestad · Morten Vassvik · Alex Hansen
PoreLab, Department of Physics, Norwegian University of Science and Technology, NTNU, N-7491 Trondheim, Norway.
E-mail: alex.hansen@ntnu.no

The problem of two-phase flow in porous media has extensively been studied using laboratory experiments [3–6, 16, 17], statistical models [8, 9, 18] and numerical simulations [4, 19]. There have been significant theoretical developments in describing the steady-state properties [20–23]. Due to the vast advancement in the computer power and development in scanning instruments for pore space reconstruction, the computational modeling techniques play a leading role in the study of two-phase flow problems. There are different modeling approaches. The direct numerical simulations, such as the volume-of-fluid method [24] and the level-set method [25, 26], perform discretization of the pore space into smaller cells and solve the Navier-Stokes equation. A popular voxel-based simulation technique is the lattice Boltzmann method (LBM) which solves the Boltzmann transport equations for different species of lattice gases at the discretized pore space [27–29]. These techniques all provide detailed information on the flow propagation at pore scale and are useful where the actual shape of the pores matter. However, due to the discretization of the pores, these models become computationally expensive when studying systems with large number of pores, such as for the scale-up problems.

Pore-network modeling [30, 31], in this regard, proves a computationally efficient method that can treat much larger systems. In pore-network modeling, a porous matrix is modeled as a network of links (pore throats) that are connected at nodes (pore bodies). The actual shapes of the pore space are replaced with simplified geometries and the average flow properties for each pore is considered to model the flow of the system. Unlike the voxel-based methods that discretize the pore space in smaller grids, here one pore is the smallest computational unit in the pore-network simulations. This simplification loses the detailed evolution of the fluid arrangements inside a pore, however it allows the pore-network models to apply for large systems and thereby study their statistical properties. There are two main ingredients for transporting fluids in a pore-network model: (1) the local pressure drops in the pores and (2) the resulting displacements of the fluids. Based on these two ingredients, there are two major groups of pore-network models, quasi-static models and dynamic models. The quasi-static models are intended for the flow that is dominated by capillary forces so that the viscous forces can be neglected. The displacement of fluids in the quasi-static models are performed by filling a whole pore at a time with invasion percolation-type algorithms [5, 8, 32, 33] where the filling of pores are decided by capillary entry pressures or by determining the stability of an interface for a given contact angle [34, 35]. Quasi-static models can successfully describe the equilibrium properties of two-phase flow at capillary dominated regime [36–38], however they are unable to capture the dynamic effects from the interaction between viscous and capillary forces at higher flow rates. This interaction between the viscous and capillary forces at the pore scale are taken into account in the dynamic pore-network models where the fluids inside pores are displaced under both the viscous and capillary pressure drops [39–41]. The viscous pressure drops are calculated by solving flow equations for fully developed viscous flow inside the pores and the capillary pressure drops are obtained from the local fluid configuration inside a pore. There are many factors that make the dynamic models computationally more complex to implement compared to the quasi-static models and efficient algorithms are therefore necessary. One such factor is the mixing of fluids at the nodes and distributing them to the neighboring links while conserving the volumes of each fluid.

In this article, we present in detail a set of algorithms to implement the displacements of two fluids in the links of a pore network and to distribute them to the neighboring links after they pass the network nodes. Together with these algorithms, we describe an *interface-tracking* dynamic pore network model in which the location of two fluids inside the pores are marked explicitly by the positions of all the interfaces at any time step. These interfaces are displaced in small steps under the instantaneous viscous and capillary pressure drops at the pores. We therefore call the algorithms as *interface-dynamics* algorithms. The displacements of all the interfaces with time describe the transport of the fluids through the network. This is different from other pore-network models, such as in [39], where the interface positions are only available implicitly from the volumetric saturation of the fluid elements inside a pore, or from the model in [40] where an interface is moved through a whole volume element at each time step. Explicit positions of all the interfaces in this interface-tracking model provides a detailed picture of the fluid configuration at any time. Calculation of the capillary forces thus become straightforward from the interface positions and different dynamical events, such as the retraction of invasion fronts after a Haines jump [42–45], can easily be resolved.

The interface-tracking model we describe here was first introduced by Aker et al. in late nineties [41] to study transient two-phase flow – i.e. drainage – in a pore network. The interface algorithms in that model were developed for the drainage in a regular pore network with open boundaries, where a non-wetting fluid invades the network filled with wetting fluid. There, the algorithms were made in such a way that the fluid-volumes

were not conserved as they pass across the nodes. Later, the model was extended for steady-state flow by implementing periodic boundary conditions in the flow direction [46]. There the interface-dynamics algorithms of the previous model were updated to maintain the volume conservation. However, the rules to transport the interfaces through nodes described in the model were based on different events at the nodes of a regular square network in two dimension and were not straightforward to implement in an irregular network topology, such as the networks reconstructed from real samples. Since then, the model has been updated over the years and efforts have been made to generalize the rules for interface dynamics that can be applied for any type of network topology and spatial dimension, as well as for both the transient and steady-state flow [15]. However any detailed description of the new algorithms were absent. Therefore, one of the main goals of this article is to describe these new interface algorithms with sufficient details so that the reader may reproduce the model. The interface algorithms we present here are universal in terms of the network connectivity and topology and can be used for different networks without any further modification. Though these algorithms are simple and straight-forward to implement, they are capable to capture the essential physical properties of both the transient as well as of steady-state immiscible two-phase flow. We will show this by presenting a few fundamental results of transient and steady-state two-phase flow in porous media using this model. When the statistical properties are concerned, fine details of dynamics are generally dropped out. This makes it possible to model the fluid displacements with simplified interface dynamics rules, while still preserving the fundamental statistical properties of the flow.

We like to point out that, complex flow mechanisms such as the wetting films along the pore walls can also be included in the model as presented in [47]. However, we do not consider them in this article and restrict ourselves only to the simplest case of Darcy-like creep flow. Moreover, here we will use an explicit Euler integration method to do the time steps, whereas semi-implicit methods can be used for computational efficiency at very low flow rates as illustrated in [48]. A Monte-Carlo algorithm was also developed recently for this model to achieve the steady state in less computational time [49]. We also note that important phenomena such as wetting angle hysteresis is straight-forward to implement but it has not been included so far. However, wetting angle alteration due to changes in the composition of the immiscible fluids has been considered in the past [50, 51].

The article is structured as follows. In section 2, we will present the governing equations describing the two-phase flow at the pore level and will describe how we solve the equations to find the local pressures at the nodes at any time step. Then we present in detail in section 3 the interface-dynamics algorithms which transport the fluids inside the links and distribute them to the next connected links after they pass a node. The algorithms are divided into three functions, which will be presented in the subsections. In section 4, we will describe how different boundary conditions can be implemented in this model. In order to validate the model, we will present a few examples in section 5 where the model can successfully reproduce some fundamental results of two-phase flow. Both the transient and steady-state flow will be simulated and the corresponding results will be presented in the subsections 5.1 and 5.2 respectively. Finally, we will draw our conclusions in section 6.

2 Flow equations

We consider immiscible flow of two incompressible Newtonian fluids through a network of pores, where one of the fluids is more wetting than the other with respect to the pore walls. We denote the less and more wetting fluids as the non-wetting (n) and wetting (w), respectively. For a given network, two dimensionless macroscopic parameters that characterize the dynamics of two-phase flow are the capillary number (Ca) and the viscosity ratio (M). The capillary number is a measure of the ratio of viscous to capillary forces in the system. These parameters are defined as,

$$Ca = \frac{\mu_e Q}{\gamma A} \quad \text{and} \quad M = \frac{\mu_n}{\mu_w} \quad (1)$$

where Q is the total flow rate, γ is the interfacial tension between two fluids and A is the cross-sectional pore area of the network. μ_n and μ_w are the viscosities of the two phases. In case of transient studies μ_e is the viscosity of the invading phase, whereas for steady-state flow μ_e is considered as the saturation-weighted effective viscosity of the two phases. Hydraulic properties of a pore-network depend on the geometrical shape of the individual pores, as well as on the network topology, that is, the connectivity and spatial organization of the nodes and links of the network [52]. With our model, we can consider pore networks in two (2D) or three (3D) dimensions with different topologies as illustrated in figure 1. In (a), we show a crop of a Hele-Shaw cell filled

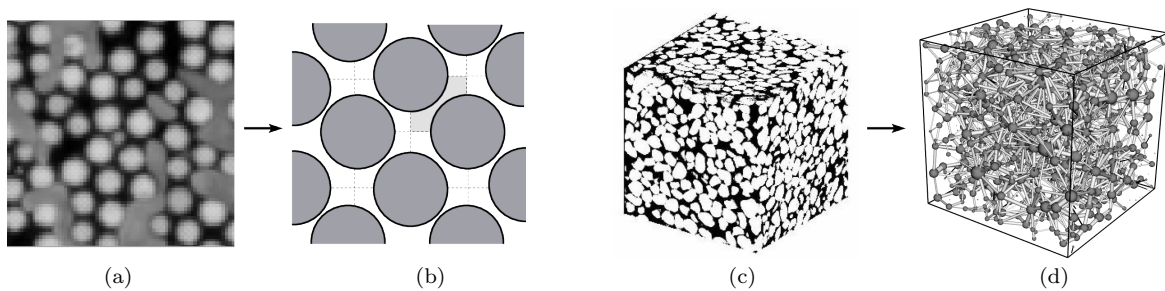


Fig. 1: An overview of the network representation of two and three dimensional porous media. Figure (a) shows a $10\text{ mm} \times 10\text{ mm}$ crop of a $42\text{ cm} \times 85\text{ cm}$ Hele-Shaw cell, filled randomly with a monolayer of 1 cm -diameter glass beads, indicated by the white circles [53]. The black and gray colors in the image show the wetting and non-wetting fluids. Such a system can be modeled by a two-dimensional network of hour-glass shaped links as shown in (b), where the distribution in link radii and node positions can be tuned according to the system properties. In (b), the dark gray circles represent the beads and white represents the pores. The links are separated by dotted lines and the intersection of two such lines defines the position of a node. One link is colored by light gray. We like to point out that, (b) is not an exact reconstruction of the image shown in (a), rather it is a simplified illustration. In (c), we show a three dimensional Micro CT image of sand-pack (sample F42A in [55]) and the corresponding reconstructed pore network is shown in (d).

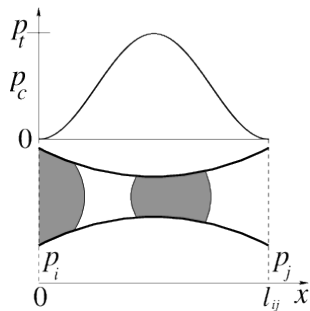


Fig. 2: Schematics of a link in the network, where the narrow throat and wide pore body is modeled by an hour-glass shape in terms of the capillary forces (p_c). The variation of p_c at an interface with its position inside the link is shown above. The wetting and non-wetting fluids inside the link are colored as white and gray respectively. Here, p_c is modeled with a cosine function, however one may consider any other function with a minimum in the middle.

with monolayer of glass beads [53] that is widely used as a two-dimensional model porous medium in laboratory experiments. Such a porous medium may modeled as a two-dimensional network of disordered pores as shown in (b). A porous medium in 3D, a sample of sand-pack [54, 55], is shown in (c) and a network that is reconstructed from the sample is shown in (d). There are different techniques for reconstructing the pore-network from scanned images of the sample, which can be found in a wide range of literature [56–60].

A pore typically consists two wider pore bodies that are connected by a narrower pore throat. In our network representation, the centers of the pore bodies provide the positions of nodes which are connected by links. In this model, we assign all the volume of the pore space to the links of the network and the nodes do not contain any pore volume. This introduces a variation in the cross-sectional area along the length of the link due to the wider pore bodies at the ends and the narrow pore throat in between. We model the cross section of the link by a simplified hourglass shape as shown in figure 2. The interfacial pressure (p_c) at an interface therefore depends on the position of the interface as it moves along the link. The functional dependence of p_c on the position, obtained from Young-Laplace equation, takes the form [61],

$$|p_c(x_k)| = \frac{2\gamma \cos \theta}{r_j} \left[1 - \cos \left(\frac{2\pi x_k}{l_j} \right) \right] \quad (2)$$

where r_j is the average radius of a link j and $x_k \in [0, l_j]$ is the position of the k th interface inside the link. Here γ is the surface tension and θ is the contact angle between the interface and the pore wall. If p_a and p_b are the local pressures at the two nodes a and b across the link, the instantaneous local flow rate q_j inside the link from node a to b is proportional to the difference between the viscous pressure drop Δp ($= p_b - p_a$) across the link

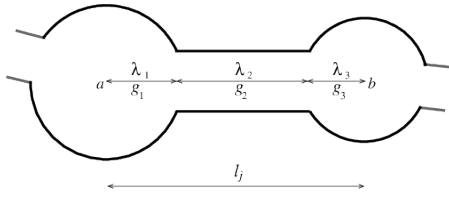


Fig. 3: Schematics of one pore in the reconstructed network which consists of three pore parts, two pore bodies at the end and a narrow pore throat in the middle. $\lambda_{1,2,3}$ and $g_{1,2,3}$ are the lengths and mobility contributions. The total length of the link $l_j = \lambda_1 + \lambda_2 + \lambda_3$ and the total mobility of the link is obtained from equation 4.

and the total capillary pressure drop due to all the interfaces inside the link. This can be calculated by [62],

$$q_j = -\frac{g_j}{l_j \mu_j} \left[\Delta p_j - \sum_k p_c(x_k) \right] \quad (3)$$

where the sum is over all the interfaces inside the link j , taking into account the direction of the capillary forces. μ_j is the saturation-weighted viscosity of the fluids present inside the link at that instant, given by $\mu_j = s_{j,n} \mu_n + s_{j,w} \mu_w$. Here $s_{j,n} = l_{j,n}/l_j$ and $s_{j,w} = l_{j,w}/l_j$ are the fractions of the link length occupied by the non-wetting and wetting fluids respectively, so that $s_{j,n} + s_{j,w} = 1$. The term g_j is the mobility of the link, which depends on the cross section of the link. This model deals with piston-like creep flow at low Reynolds number without any corner flow or film flow. In that case, the effect on q_j due to a different cross-sectional shape can be taken into account by the link mobility term g_j . For the regular network in 2D we chose the links to be cylindrical with circular cross section for which $g_j = a_j r_j^2 / 8$ for Hagen-Poiseuille flow [1], where $a_j = \pi r_j^2$ is the cross sectional area. In the reconstructed 3D network, the pores are triangular in shape and characterized by a shape factor (G), defined as the ratio between the effective cross-sectional area of the pore and the square of its circumference. The effective cross sectional areas of each of the three pore parts, the two wider pore bodies at the ends and the narrow throat in the middle, are calculated from the relation $\alpha = \rho^2 / (4G)$, where ρ is the radius of the inscribed circle in that pore part [63]. The mobility contribution from each part of the pore is then obtained from the relation $g = 3\rho^2 \alpha / 20$ [64, 65] and the mobility term g_j for the total link is then calculated from the harmonic average of the contribution from the three individual terms given by,

$$\frac{l_j}{g_j} = \frac{\lambda_1}{g_1} + \frac{\lambda_2}{g_2} + \frac{\lambda_3}{g_3} \quad (4)$$

where $\lambda_{1,2,3}$ and $g_{1,2,3}$ are the lengths and mobility of the each pore parts respectively as shown in figure 3.

In order to move the fluids through the pores, the local pressures at nodes are needed to be solved at each time step. The net volume flux (f_i) through every node at each time step will be zero with the Kirchoff equations, therefore for any node i ,

$$f_i = \sum_h q_h = 0, \quad (5)$$

where the subscript h runs for the links connected to the node i . This sum, along with the equations 2 and 3, constructs a set of linear equations. We solve these equations with conjugate gradient solver [66] or the Cholesky factorization method [67] and the solutions of which at any time step provides the local node pressures p_i at that step. The system can be driven by a constant global pressure drop ΔP or a total flow rate Q with open or periodic boundary conditions. More details about implementing different boundary conditions will be presented in section 4.

3 Interface-dynamics algorithms

We specify the locations and displacements of the two fluids inside the pore space by the positions of all the interfaces. Transport of the fluid bubbles through the links, the coalescence and the snap off of the bubbles – all are treated by the interface-dynamics algorithms by the displacement, creation and deletion of the interfaces. The underlying idea of these algorithms are very simple, at every time step we calculate the volumes of fluids arriving at each node from incoming links and then distribute them to the outgoing links with the volumes proportional to the flow rates in them. In our implementation, the full algorithm for the interface dynamics is sub-divided

into three intermediate functions, we name them (a) `interface_move`, (b) `interface_create` and (c) `interface_merge`. Each of these functions is applied at every time step. The purpose of `interface_move` is to move every interface in each link according to the local link flow rate and to measure the amount of fluids that enter to a node from all the connected links with incoming flow. Next, the `interface_create` function displaces all the accumulated fluids from each node to the connected links that have the outgoing flow and creates new interfaces at the entrance of those links. Finally the `interface_merge` function controls the maximum number of interfaces in any link, which can be viewed as an equivalent of the merging and mixing of fluids at the nodes. These three intermediate steps are applied at every links and/or nodes at each time step which together manage the whole process of fluid displacements. We describe them in the following and illustrate them in Fig 4. When describing the algorithms, we will show simulation results at limiting values of parameters to make sure that the rules do not produce any unphysical results. This also helps to select the best possible rule for an algorithm when there can be a few different choices.

3.1 `interface_move`:

The pore network consists of N_L number of links that are connected to each other by N_N number of nodes. We will use the subscript i for a node ($i = 1, \dots, N_N$) and the subscript j for a link ($j = 1, \dots, N_L$). The interface number inside a link is denoted by k . Inside the code, one also needs to mark the type of the interfaces, for example, whether it is an interface at the beginning of a non-wetting bubble or at the end. This is necessary in order to calculate the direction of the capillary forces and also to measure the amount of two individual fluids that enter from a link to node. Whether it is a regular network with constant coordination number for each node or an irregular network where the nodes have different coordination numbers, such as a reconstructed network from a real sample, it does not change any of the rules described in the following. In figure 4, we illustrate them for an example of five links connected to a node i . At a time step, when all the pressures (p_i) at the nodes for an existing fluid configuration are known from the solutions of Kirchhoff equations, the flow rates q_j inside the links are obtained from equation 3. A time interval (Δt) is then decided in such a way that an interface inside any link does not move more than 10% of corresponding link length at that time step. In order to do so, the link-velocities c_j are calculated from local flow rates q_j by $c_j = q_j/a_j$, where a_j is the cross sectional area of the link j . The time step is then calculated as

$$\Delta t = \frac{0.1l_j}{c_{j,\max}}, \quad (6)$$

where $c_{j,\max}$ is the largest fluid velocity among all the links and l_j is the length of that link. For the time evolution, we use an explicit Euler-type procedure. This works well for a large range of capillary numbers with only the time step criterion mentioned in equation 6. In order to ensure numerical stability at low capillary numbers, however, the sensitivity of interfacial pressure jumps to perturbations in interface positions must also be taken into account when choosing the time step, see [48]. This puts a limit on the maximum time step size that is independent of flow rate and thus becomes a severe criterion when flow rates are low. In [48], computational efficiency was improved at low capillary numbers by a semi-implicit method. Here, however, we consider only capillary numbers that are large enough for equation 6 to be sufficient to ensure numerical stability.

After deciding the time step, interfaces inside each link j are to be moved in the direction of q_j by a distance,

$$\Delta x_j = \frac{q_j}{a_j} \Delta t \quad (7)$$

as shown in figure 4(b). Here, the links have uniform cross-sectional area in terms of the mobility, so all the interfaces inside the same link move by the same distance. The positions of all the interfaces inside any link ($x_{j,k}$) are then updated, $x_{j,k} = x_{j,k} + \Delta x_j$. By doing this, if any of the interfaces moves outside any link ($x_{j,k} > l_j$), it is deleted from the list of interfaces. The set of p_i s at the nodes decide which links, among all the links connected to a node, have fluids that flow towards the node and have fluids that flow away from the node at that time step. We name these links respectively as the *incoming links* and the *outgoing links* for that node. A typical example is shown in figure 4(a) for five links connected to a node i . Due to the displacement of the interfaces by an amount Δx_j , a node i receives a certain volume ($\phi_{i,j}$) of wetting and/or non-wetting fluids

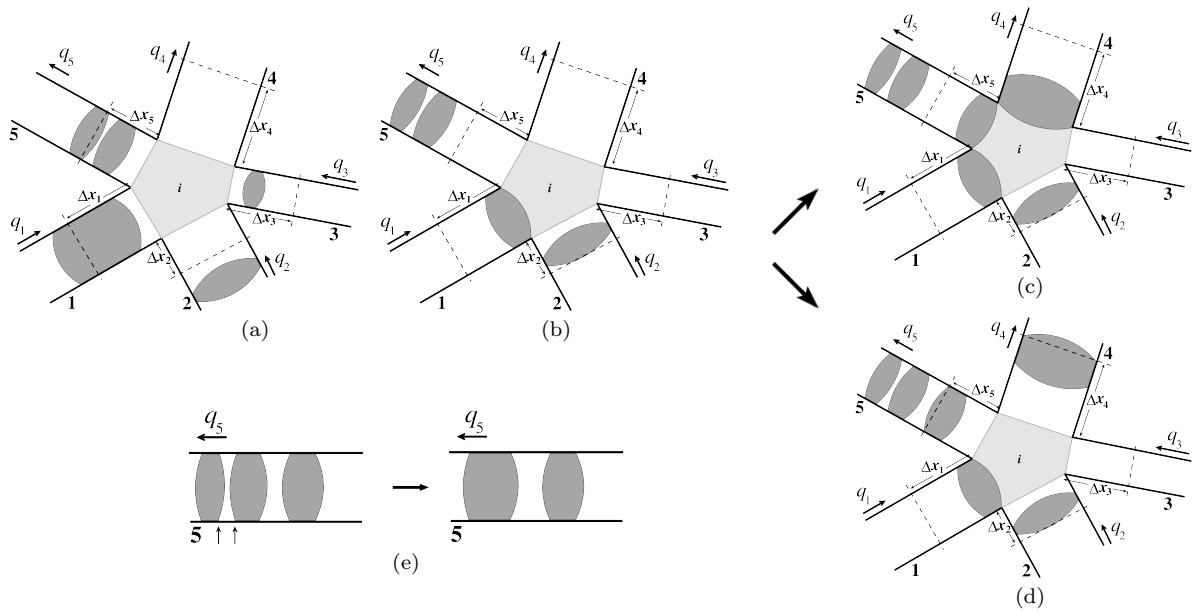


Fig. 4: The three intermediate steps for the interface dynamics, the `interface_move`, `interface_create` and `interface_merge`, at every time step are illustrated here. Here five links, numbered as $j = 1, 2, 3, 4$ and 5 , are connected to the node i . However the above illustrations are also valid for any number of links. Wetting and non-wetting fluids inside the links are colored by white and dark gray respectively. All of the pore space are distributed to the links in this model and the area around the node i , colored by light gray, does not contain any real volume. (a) shows an example configuration of two fluids at a time step. Solution of the Kirchhoff equations as described in section 2 provides the local flow rates q_j . Based on the directions of q_j at this time step, say the links 1 and 2 are identified as the incoming links whereas 3, 4 and 5 are identified as the outgoing links here. Values of the displacements Δx_j for each link, calculated from $\Delta x_j = q_j \Delta t / a_j$ (see text) are shown by dashed lines. Every interface in a link j are moved towards (in the incoming links) or away from (in the outgoing links) the node by a distance Δx_j which is shown in (b). This is performed by the function `interface_move`. The total volume of the fluids ($a_1 \Delta x_1 + a_2 \Delta x_2$) which left the links 1 and 2 into the node i is now to be placed at the beginning of the links 3, 4 and 5, which will fill the volume $a_3 \Delta x_3 + a_4 \Delta x_4 + a_5 \Delta x_5$ and will create new interfaces in the outgoing links as described in `interface_create`. There are two different ways of creating the new interfaces, one is to place the wetting fluid first and the non-wetting next as shown in (c), and the other is to place the non-wetting fluid first and the wetting next as shown in (d). We adopt (c) and (d) alternatively at each consecutive time steps. (e) shows the `interface_merge` function for the link 5 when there are four allowed interfaces. There link 5 has total 6 interfaces before merging and the two bubbles around the two nearest interfaces marked by the arrows are merged. The merging process are illustrated in more detail in figure 5.

from an incoming link j , given by $\phi_{i,j} = a_j \Delta x_j = q_j \Delta t$ that leaves from the end of the incoming link j . The total volume of fluids (V_i) received by a node i from all of its incoming links is therefore,

$$V_i = \sum_{j \in I} \phi_{i,j} = V_i^w + V_i^n, \quad (8)$$

where V_i^w and V_i^n respectively are the total volume of wetting and non-wetting fluids arrived from all the incoming links to the node i . Here $j \in I$ denotes the set of all the incoming links connected to i . We point out that, in order to apply this `interface_move` function for the whole network, one can loop through all links j , move the interfaces by the distance Δx_j and add up the amount of fluids that exit from the link to the connected node in the direction of the link-flow. This will produce the arrays of V_i^w and V_i^n the end of the loop

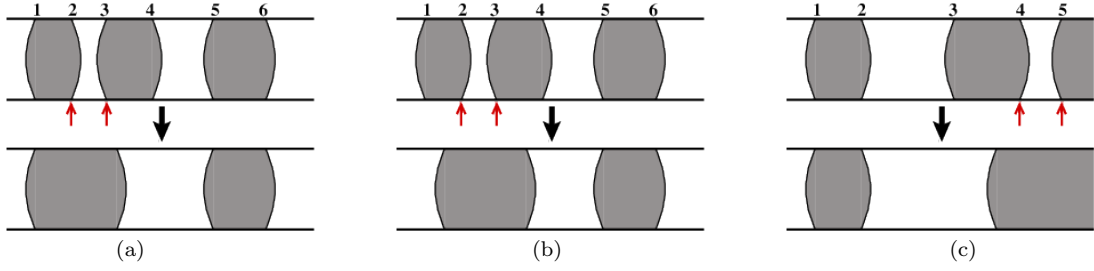


Fig. 5: Illustration of the `interface_merge` function for maximum interface count $N_{\max} = 4$. The top row shows the interface positions before merging and the bottom row shows after merging. White and gray represent the two fluids inside the links. The nearest two interfaces are indicated by red arrows. In (a) we show the simplest possible try, namely the `merge_back` scheme. The link had 6 interfaces before merging among which the interfaces 2 and 3 are the nearest. We merge them by moving only one bubble towards the another, so the interface 1 does not change its position, only the interface 4 is moved towards 1 by a distance that is equal to the distance between 2 and 3. In (b) we show the next possible try, namely the `merge_cm`. Here instead of moving the interface 4 towards 1, we move both 1 and 4 towards each other by such distances so that the center of mass of the two bubbles do not change after merging. The third and final interface merging scheme is `merge_cmnn`, which is same as (b) with an additional criteria as illustrated in (c). In the situation when one of the two nearest bubbles is connected to a node, such as the non-wetting bubble connected to the interface 5 in (c), it will get disconnected from the node according to the merging scheme (b). We avoid this disconnection of any bubble from a node by moving only the other bubble in such a situation as shown in (c). So the to merge the nearest interfaces 4 and 5, we only move the interface 3 towards the node. The `merge_cmnn` scheme is therefore a combination of (b) and (c) which we adopt here.

which contain the incoming volume flux at each the nodes at that time step. The marking of the interface types, as mentioned before, will allow here to calculate the individual terms V_i^w and V_i^n . This is illustrated in figure 4.

3.2 `interface_create`:

After the function `interface_move` is performed over all the links, the list of volumes V_i^w and V_i^n of incoming fluids for all the nodes are generated for that time step. As all of the pore space in this model is assigned to the links of the network and the nodes do not contain any physical volume, the total volume of incoming fluids (V_i) to a node are to be injected at the beginning of the outgoing links at the same time step. This will create new bubbles and interfaces at the beginning of the outgoing links. The total volume of fluids that will enter from a node i to an outgoing link j is given by, $\phi_{i,j} = q_j \Delta t$, and due to the balancing of the Kirchhoff equations it ensures that $\sum_{j \in I} \phi_{i,j} = \sum_{j \in O} \phi_{i,j}$ where $j \in I$ and $j \in O$ respectively denote the set of all incoming and outgoing links for the node i . However, we still need to find out the volumes of each individual fluid for any outgoing link, that is, how much of the wetting ($\phi_{i,j}^w$) and the non-wetting ($\phi_{i,j}^n$) volumes will enter into j . We adopt a “democratic” rule to calculate this, that means both the wetting and non-wetting fluids get the same preference and the volumes depend only on the flow rate q_j of the respective outgoing link. For any outgoing link j , $\phi_{i,j}^w$ and $\phi_{i,j}^n$ are therefore calculated as,

$$\phi_{i,j}^w = q_j V_i^w \Delta t / V_i \quad \text{and} \quad \phi_{i,j}^n = q_j V_i^n \Delta t / V_i \quad (9)$$

which imply that the ratio of the volumes of a fluid among all the outgoing links are the same as the ratio between flow rates among those links. Distributing the fluids in this way also preserves the volume conservation of *each individual fluid*, that is,

$$\sum_{j \in O} \phi_{i,j}^w = V_i^w \quad \text{and} \quad \sum_{j \in O} \phi_{i,j}^n = V_i^n. \quad (10)$$

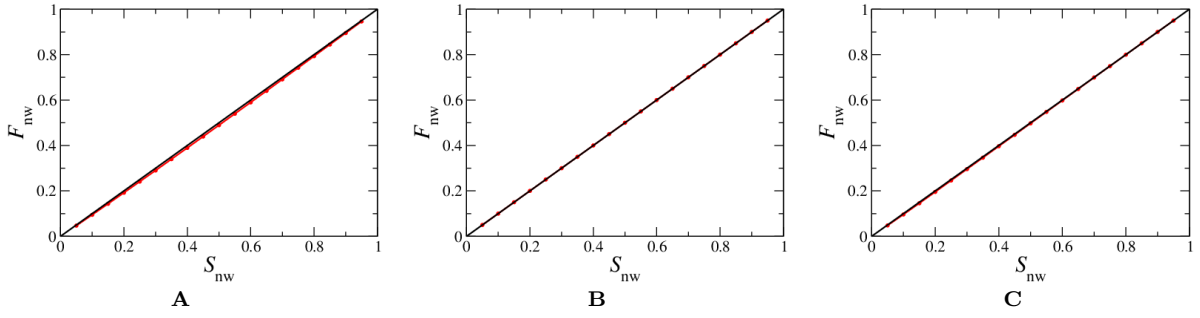


Fig. 6: Plot of steady-state non-wetting fractional flow F_n as a function of non-wetting saturation S_n for zero capillary pressure at the interfaces. The three plots correspond to the three merging schemes (A) `merge_back`, (B) `merge_cm` and (C) `merge_cmnn` as described in the section 3.3. A small but systematic deviation from the diagonal $F_n = S_n$ line can be observed for A.

In each link, the wetting and non-wetting bubbles can be placed in two different ways, the non-wetting fluid at the beginning and the wetting fluid at the next, as shown in figure 4(c) or in the other way as shown in figure 4(d). Here we adopt (c) or (d) alternatively at every consecutive time steps. One can also chose (c) or (d) randomly at every time step. This is equivalent of assuming that at some time step the wetting fluid coming from the incoming nodes pass the node before the non-wetting fluid enters the node, and the situation is the opposite in the other case.

These “democratic” rules are symmetric in terms of the wetting and the non-wetting fluids. Therefore when the surface tension is set to zero, the capillary forces will disappear and one should obtain [68],

$$Q_w(S_w, M) = Q_n(1 - S_w, 1/M) \quad (11)$$

where Q_n and S_n are the total non-wetting flow rate and the non-wetting saturation. Moreover, if we further set $\mu_w = \mu_n$ when the surface tension is zero, we should obtain,

$$F_w = S_w \quad (12)$$

Where, $F_n = Q_n/Q$, the non-wetting fractional flow in the steady state. These conditions can be used as preliminary tests for the interface functions and to verify their implementations in the code. The precise way to measure the fractional flow and other measurable quantities will be presented in section 5.

3.3 `interface_merge`:

Creating new interfaces in the outgoing links using the `interface_create` function can increase the number of bubbles inside a link indefinitely with time. In a real system, coalescence of bubbles occur inside the pores which prevents the number of interfaces from increasing indefinitely. The limit depends on the pore geometry such as the aspect ratio as well as on the flow parameters such as the capillary number and surface tension [69]. To limit the number of interfaces inside a link in our model, we use an `interface_merge` function which merges two bubbles when the number of interfaces inside a link exceeds a maximum number (N_{\max}). After the two functions `interface_move` and `interface_create` are executed for each link, we look for any link in which the number of interfaces exceeds the maximum number N_{\max} . Notice that, limiting the number of interfaces inside a link does not necessarily impose any restriction on the minimum or maximum size of a bubble. The merging of interfaces can be viewed as the coalescence of fluids during they pass the nodes. However, it is a crucial step to formulate how exactly we merge bubbles inside a link so that the volume of the two fluids remain conserved and it does not introduce any artificial effect on the flow properties.

We start with a simple rule **A** (`merge_back`), where we identified two nearest non-wetting bubbles inside a link. Among these two non-wetting bubbles, only one, say the one in the front towards the flow direction, is moved back towards the other bubble and then merged. The length of this merged non-wetting bubble is

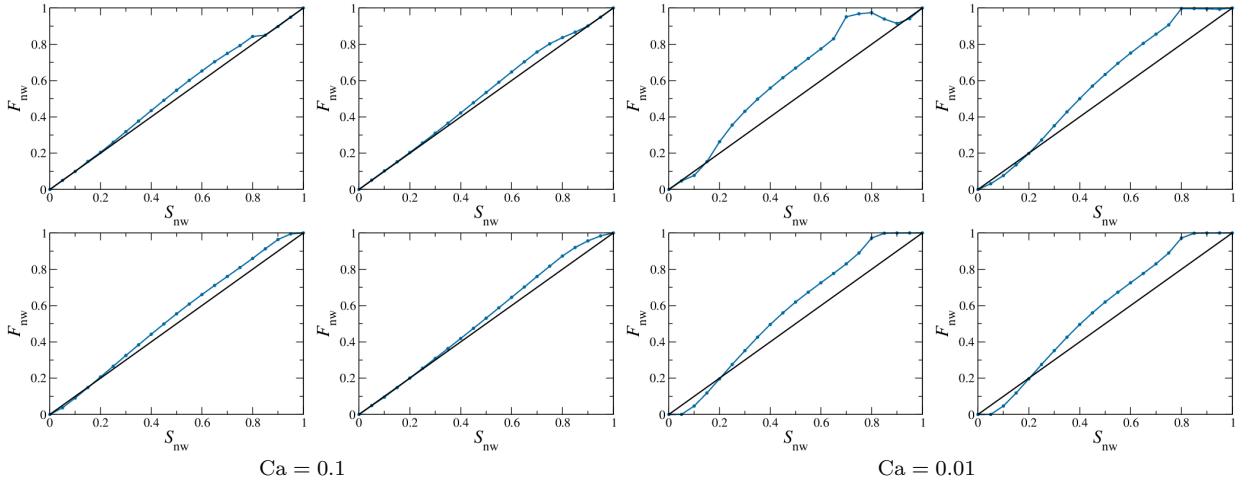


Fig. 7: Steady-state fractional flow at finite capillary numbers $Ca = 0.1$ and 0.01 with the merging rules **B**: `merge_cm` (top row) and **C**: `merge_cmnn` (bottom row). The left and right plots for each capillary number correspond to $N_{\max} = 2$ and 3 respectively. With **B**, F_n approaches towards the diagonal line at higher saturation $S_n > 0.8$ for the first three plots.

then sum of the two non-wetting bubbles before merging. This reduces the interface count by two inside the link and the other interface positions are updated accordingly. This is illustrated in figure 5 (a). However, when we measure the non-wetting fractional flow for zero surface tension with equal viscosities of the fluids, we find a deviation from equation 12. This is shown in figure 6 (a) where a small but systematic deviation from the diagonal $F_n = S_n$ line can be observed. This effect appears due to displacing the non-wetting bubble opposite to the flow which introduces a decrease in the non-wetting fractional flow. We then tried the next rule **B** (`merge_cm`), where instead of merging two nearest non-wetting bubbles, we identified any two nearest interfaces and merge the two bubbles across them. With this process, both the non-wetting or wetting bubbles can be merged whichever are the nearest. Moreover, instead of moving only one bubble towards the other, here we moved both the bubbles towards each other by such a distance so that the center of mass of these two bubbles does not change after merging. We illustrate this in figure 5 (b). This rule shows satisfactory $F_n = S_n$ behavior at the zero capillary pressure as shown in figure 6 (b). However, when we measured F_n at finite capillary numbers $Ca = 0.1$ and 0.01 , we see some discrepancy in the qualitative behavior. The results are shown in the top row of figure 7 with different maximum bubble counts $N_{\max} = 2$ and 3 . The F_n versus S_n plot generally shows an S-shaped curve for finite Ca . There the fluids need to overcome the capillary barriers at the narrow pore throats and they flow with different velocities. The phase with larger volume fraction wins and as a result the non-wetting fractional flow curve stays under the diagonal for lower non-wetting saturation and stays above the diagonal for higher non-wetting saturation. Due to the asymmetry between the wetting and non-wetting phases, the curve does not cross the diagonal at the middle. This makes fractional flow curve S-shaped when plotted against the saturation. When the saturation of a fluid is very high, it percolates through the system by trapping the other fluid in small clusters and the fractional flow of the percolating fluid become close to 1. However, for the merging scheme `merge_cm` (**B**), we see that at higher saturation values ($S_n > 0.8$), the curve again approaches to the diagonal line. We do not see any physical reason for this behavior other than an artificial effect introduced by the merging scheme **B**. It seems that, as we moved both the bubbles towards each other while merging, small bubbles connected to different links at the nodes got disconnected and started flowing. We therefore updated the merging scheme further on. In the third and final rule **C** (`merge_cmnn`), we added one additional criteria compared to **B**. There we made sure that any fluid bubble that is in contact to a node, does not get disconnected from the node during the merging process. In order to do so, if one of the two nearest bubbles are connected to a node, we did not move that bubble during the merging process and only moved the other one. Everything else in this rule **C** are the same as rule **B**. With this merging scheme, we found exact match of fractional flow with equation 12 at zero surface tension and also obtained the expected

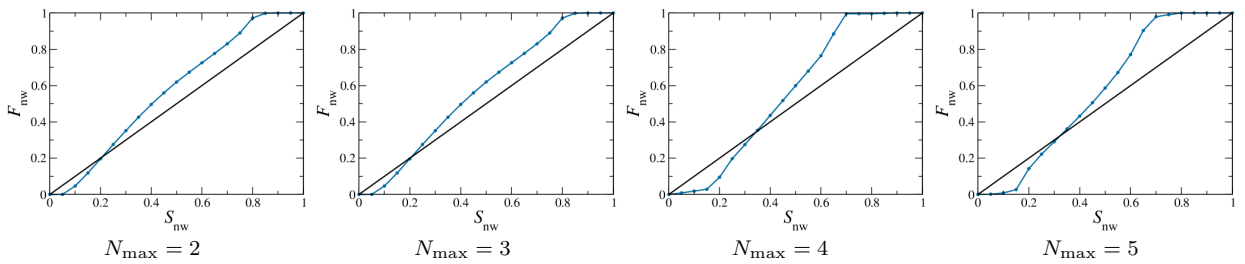


Fig. 8: We show the effect of changing the maximum number of interface (N_{\max}) with the merging scheme **C**, the `merge_cmnn`. The steady-state non-wetting fractional flow is plotted as a function of non-wetting saturation for $N_{\max} = 2, 3, 4$ and 5 . With such a change in the interface count, no noticeable difference is observed in the qualitative behavior in F_n .

qualitative behavior for non-zero capillary pressure. These are shown in figure 6 (c) and in the bottom row of figure 7 respectively. Moreover, while changing the maximum bubble count with this merging scheme, we find no noticeable difference in the qualitative behavior of F_n with the change in N_{\max} . This is shown in figure 8 for $N_{\max} = 2, 3, 4$ and 5 . We therefore finally adopt the `merge_cmnn` as the merging scheme.

4 Boundary conditions

Simulations of different types of flow need proper boundary conditions to be implemented. The drainage displacement simulations can be performed with open boundary conditions (OB) where two opposite edges can be used as the *inlets* and *outlets* and the other edges are kept closed. Depending on the setup, all or some of the nodes and links at the inlet edge can be considered to inject a fluid. Depending on whether the system is driven under constant pressure drop or constant flow rate, either the node pressures (p_i) or the link flow rates (q_j) at the inlets are to be set externally. We also need to set the node fluxes (V_i^w and V_i^n) at the inlets depending upon the type of fluid injected. For the injection of non-wetting fluid, all the V_i^n s are set to be one and the V_i^w s are set to be zero for all the inlet nodes. With these, we solve the equations for pressures and flow rates for all the other nodes and links inside the network.

The open boundary conditions can also be used for steady-state flow for the setup that is generally used in laboratory experiments [12]. There, instead of injecting one fluid, two fluids are injected simultaneously through alternate inlets. For this setup, all we need to do is to set the inlet node fluxes accordingly, all the V_i^n s are set to one for the non-wetting inlets and all the V_i^w s are set to one for the wetting inlets. The inlet flow rates define the total flow rate (Q) and the fractional flow $F_n = Q_n / (Q_n + Q_w)$. Here, $Q_n = \sum'_n q_j$ and $Q_w = \sum'_w q_j$ where \sum'_n and \sum'_w indicate the sum over all non-wetting and wetting inlets respectively. The fractional flow F_n is an external parameter in this setup and the saturation S_n is decided by the system.

There is a better way to run steady-state flow in the simulations which is not possible in case of the experiments. This is by implementing the periodic boundary (PB) conditions in the direction of overall flow. For this, we connect the inlet and outlet edges so that the fluids leaving at the outlets, enter the system again through the inlets. The links that connect the inlets and outlets, we call *ghost links*. With this, the network becomes a closed system and the two fluids keep flowing through the system. The saturation S_n therefore is an external parameter here and the fractional flow is decided by the system. This is illustrated in figure 9 for 2D and 3D networks. In case of 2D, periodic boundary conditions are applied in both directions which makes the flow equivalent to the flow on the surface of a torus as shown in (b). For the reconstructed network in 3D, the opposite inlet and outlet edges are not identical. Therefore, to apply to periodic boundary conditions to this network we double the system by a mirror copy of the network in the direction of the flow, as shown by the two cuboids in (d). This makes the inlets and outlets at the opposite edges identical, which we then connect with the ghost links to make the system periodic. With the periodic boundary, the inlets are seen as the neighbors of the outlets for the interface-dynamics algorithms. Here, the global pressure drop ΔP to drive the flow needs to be added with the node pressure drops across the ghost links while solving the equations 3 and 5.

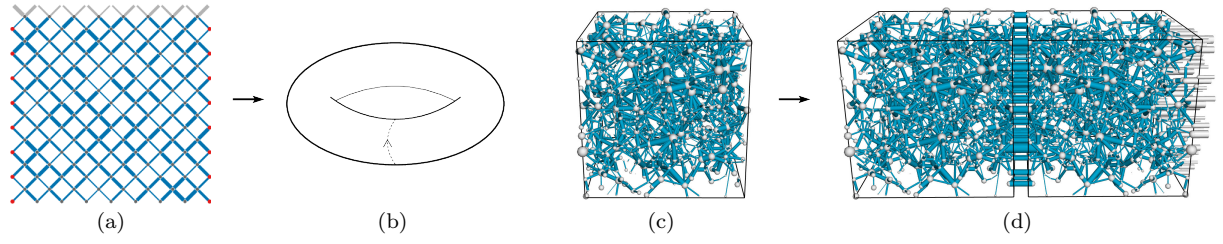


Fig. 9: Implementation of periodic boundary conditions for 2D and 3D networks. A 2D regular network is shown in (a) where periodic boundary conditions are applied in both the directions. Here the overall flow is in the upward direction and the gray links at the top row represent the ghost links. The links are hourglass shaped in terms of the capillary pressure, but indicated here by uniform tubes for the simplicity of drawing. The nodes are marked by small dots where the red dots at the left and right edges represent identical nodes. This makes the flow essentially on the surface of a torus as shown in (b) where the arrow represents the effective flow direction. For 3D, a network reconstructed from Berea sandstone is shown in (c) where the overall flow is from left to right. Periodic boundary conditions are applied in the direction of flow by adding a mirror copy of the the network as shown in (d). The ghost links at the right are colored by gray.

The structure of the complete simulation with all the interface dynamics functions is the following:

```

1: Network: construct or read
2: Define: boundary conditions
3: Initialize: random or sequential fluid distribution
4: for  $t = 1$  to timesteps do
5:   Solve the pressure field
6:   for  $j = 1$  to totallinks do
7:     interface_move(j)
8:   end for
9:   for  $j = 1$  to totallinks do
10:    interface_create(j)
11:    interface_merge(j)
12:   end for
13:   Calculate measurable quantities at  $t$ 
14: end for

```

During initialization, the initial positions of all the interfaces in each link will be defined depending on the saturation and how we want to start the simulation. Then after solving the pressure field, the `interface_move` function is performed on all the links and that will generate the array of the node fluxes V_i^w and V_i^n for each node i . These arrays will then be used as input to the `interface_create` function that will create the new interfaces in the links.

5 Applications and validation

As stated earlier, the interface algorithms in this pore-network model has the flexibility to be applied for different network topologies and boundary conditions. Moreover, we can study both the transient and the steady-state properties. In our simulations, we consider a network of links forming a tilted square lattice at an angle 45° with the direction of applied pressure drop in 2D. The length of each link (l_j) is 1 mm and their radii (r_j) are taken from a uniform distribution of random numbers in the range from 0.1 mm to 0.4 mm. In 3D, we consider a network that is reconstructed from a real sample of Berea sandstone by using micro-CT scanning [54, 55]. The reconstructed network contains 2274 links that are connected via 1163 nodes and has a physical dimension of 1.8^3 mm^3 . We doubled this network by adding a mirror image of itself in the direction of the applied pressure drop in order to apply periodic boundary conditions. In the following, we present some of the fundamental

results of transient and steady-state of two-phase flow in porous media by using this pore-network model. All the following results are obtained only by changing the parameters values and the boundary conditions as necessary, while using the exactly same code for the interface dynamics algorithms.

5.1 Drainage displacements

As described in the introduction, when a non-wetting fluid is invaded into a porous medium filled with a wetting fluid, it generates different types of invading flow patterns depending on the capillary number and viscosity ratio. A less viscous fluid displacing a high viscous fluid creates viscous fingering patterns at a high Ca [6, 17] and capillary fingering patterns at low Ca [7]. The capillary and viscous fingering patterns resembles with the invasion percolation [8] and diffusion limited aggregation (DLA) models [9] respectively. Alternatively, when a high viscous fluid displaces a low viscous fluid, a stable displacement front is observed. In order to verify whether our pore-network model can reproduce these different flow patterns during the drainage, we run different simulations for different values of the capillary number Ca and viscosity ratio M . In our simulations, we set $\gamma \cos \theta = 0.03$ N/m. The results are highlighted in figure 10. Here $M = \mu_n / \mu_w$ where μ_n and μ_w are the viscosities of the invading blue fluid and the wetting gray fluid. In the top row the low viscous non-wetting fluid displaces the more viscous fluid where one can observe the development of the viscous fingering pattern. In the second row $M = 10^2$, and a more viscous blue fluid is displacing the less viscous gray fluid and a compact and stable displacement front is observed [5]. Flow patterns in the third row correspond to capillary fingering which are generated with the simulations at a very low capillary number $Ca = 10^{-5}$. These fingering patterns are more fractal than the viscous fingering and depend strongly on the system disorder. We like to point out that, these three different transient regimes are generated only by altering the values of the flow rate Q and the viscosities of the two fluids to set the values of Ca and M , and no modification in the interface dynamics algorithms were made between different simulations.

5.2 Steady state

Steady-state flow can be simulated by implementing either open or periodic boundary conditions. In figure 11, we show the evolution of the system to reach the steady state at a constant flow rate with different boundary conditions. The top row shows simulations with open boundary condition, where wetting (gray) and non-wetting (blue) fluids are injected through alternate injection points at the bottom edge of a two-dimensional pore network consisting 64×100 links. The radii (r_j) of the links are drawn from a uniform random number distribution in the range $0.1l$ to $0.4l$, where l_j is the length of the links. The top edge of the network is kept open, through which fluids leave the system. The two side edges are connected with periodic boundary here but can also be kept closed if necessary. We can control the flow rates of the individual fluids which sets the fractional flow. Here the simulations are shown for $F_w = 0.5$. As there will be traces of injection of the alternate fluids near the inlet edge, one consider a system that is long enough in the direction of the overall flow so that a region of spatially homogeneous steady-state flow can be achieved away from the inlets. At the right, we plot the average global pressure drops as a function of the injected pore-volumes which show the evolution to the steady state when ΔP fluctuate around an average value. The second row of figure 11 shows simulations with periodic boundary conditions in a disordered square lattice of 64×64 links. Here the system is closed and the control parameter is the fluid saturation. The simulations are shown for $S_w = 0.5$. In the bottom row, we show the simulation with a three dimensional pore network reconstructed from a real sample of Berea sandstone for $S_w = 0.5$.

In the following, we present two examples of simulation results with this dynamic pore network model to show excellent agreement with the steady-state properties of two-phase flow. First, we will present the effective rheological properties where the total flow rate shows non-linear dependence on the pressure drop in the capillary dominated regime [12–15]. Next, we measure seepage velocities and will verify the relations between them [23]. We will also describe in detail how to measure different quantities of flow, such as the flow rates and the seepage velocities of the different fluid components.

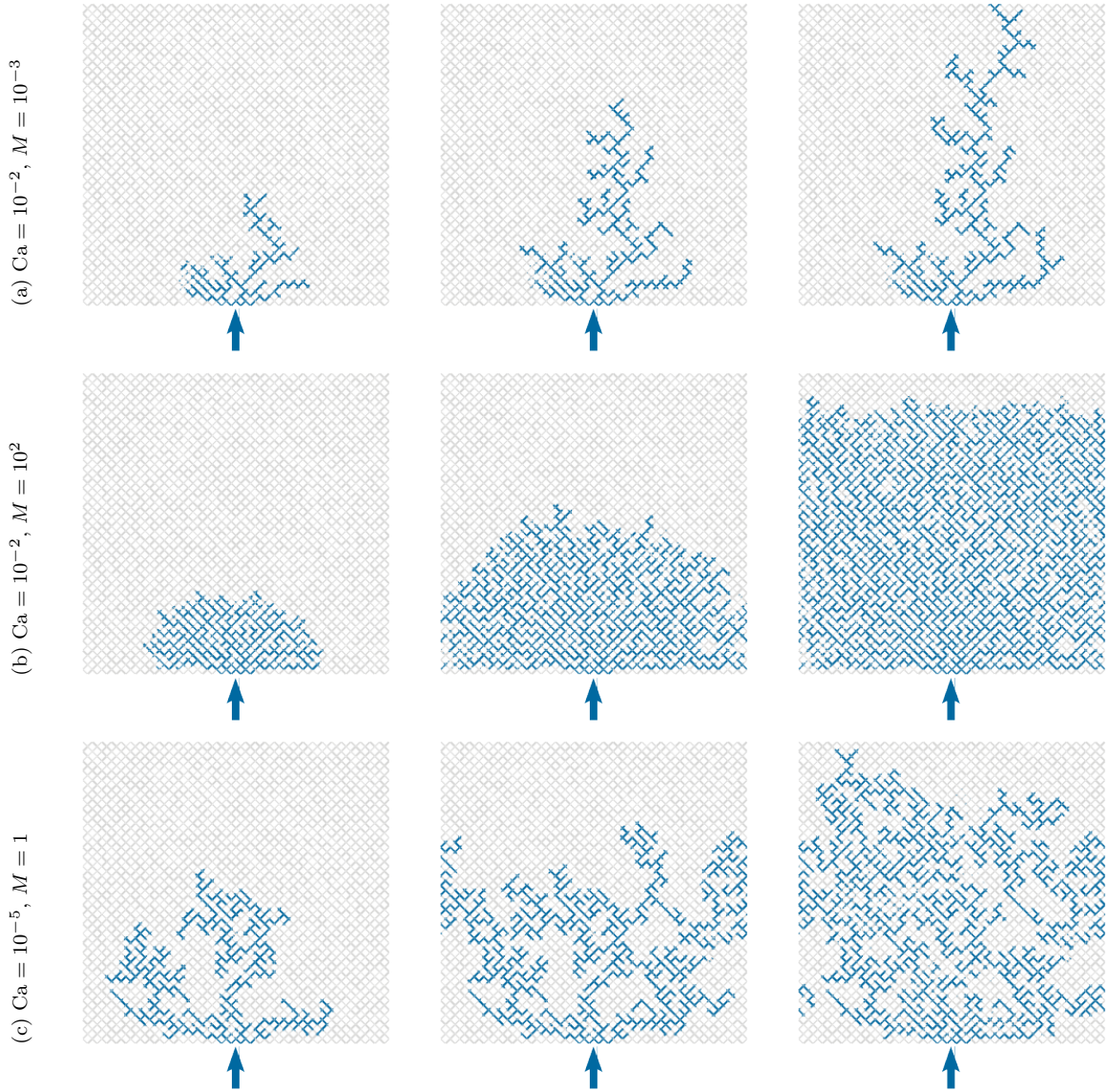


Fig. 10: Development of transient flow patterns during the drainage simulations in a disordered square network of 64×64 links. The network is initially filled with wetting fluid (gray) and the non-wetting fluid (blue) is injected through four inlet nodes at the bottom edge of the network, shown by the arrow, with a constant flow rate. The top edge of the network is kept open which works as the outlet. Periodic boundary conditions are applied in the horizontal direction, therefore the left and right edges are connected together. Only the capillary number Ca and the viscosity ratio M are altered during these simulations and all other flow parameters and the algorithms for interface dynamics are exactly the same. The flow patterns show the different regimes of transient two-phase flow, namely (a) the viscous fingering (b) the stable displacement and (c) the capillary fingering. We like to point out that, though we adopted “democratic” rules for interface algorithms, it is the solution of the flow equations that lead the fluids to generate these different flow patterns.

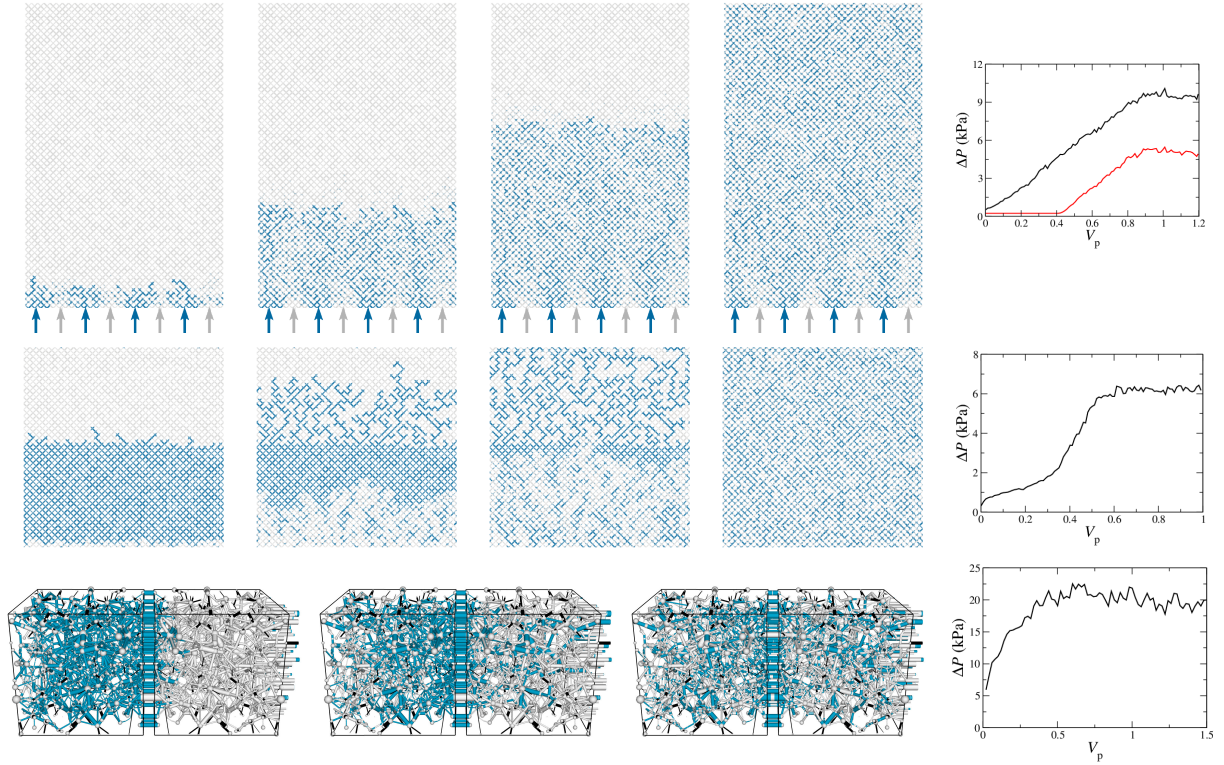


Fig. 11: Evolution to the steady state under different boundary conditions. All the simulations are performed at constant flow rate with $Ca = 0.001$ and $M = 1$. The wetting and non-wetting fluids are colored by gray and blue. In the first row, simulations with open boundary conditions with a 2D square network of 64×100 links are shown, where two fluids are injected through alternate injection points at the bottom inlet row, as shown by the arrows of two different colors. The fractional flow is $F_n = 0.5$ here which is controlled by defining flow rates at the inlet links that act as boundary conditions while solving the flow equations. The top outlet row is kept open. The second row shows the steady-state simulation with periodic boundary conditions with a 64×64 links. Saturation is a control parameter here and $S_w = 0.5$ in these simulations. In the third row of figures, we show steady-state simulations with reconstructed 3D networks from Berea sandstone where the overall flow is the direction from left to right. At the right, we plot the global pressure drops of the respective systems as a function of the pore volumes of fluids that passed through any cross section where the red and black plots for the first system show the average pressure drops at the middle and at the inlet of the system with respect to the outlet row.

5.2.1 Effective rheology and crossover from linear to non-linear flow regime

Experiments have shown that the two-phase flow in the steady state do not follow the linear Darcy relation between the total flow rate and the pressure drop in the steady state in capillary dominated regime [11–13]. The capillary pressures at the interfaces in two phase flow create threshold barriers. The distribution of these thresholds over the system depends on the pore sizes as well and on the interface configurations in the steady state, which in turn depend on the flow dynamics. These threshold pressures create a global yield threshold pressure (P_t) below which there is no flow through the system. Above P_t , the pores start opening while increasing the pressure drop, due to which the total flow rate no longer vary linearly with the pressure drop ΔP and shows non-linear behavior. This non-linear behavior depends on the distribution of the threshold pressure as well as on the system geometry [70]. For two Newtonian fluids flowing through a porous media, it was found experimentally [11–13, 15], numerically [14, 15] and with mean field calculations [14] that, in the regime when capillary pressures compete with the viscous forces, that is, in the low capillary number regime, the total flow

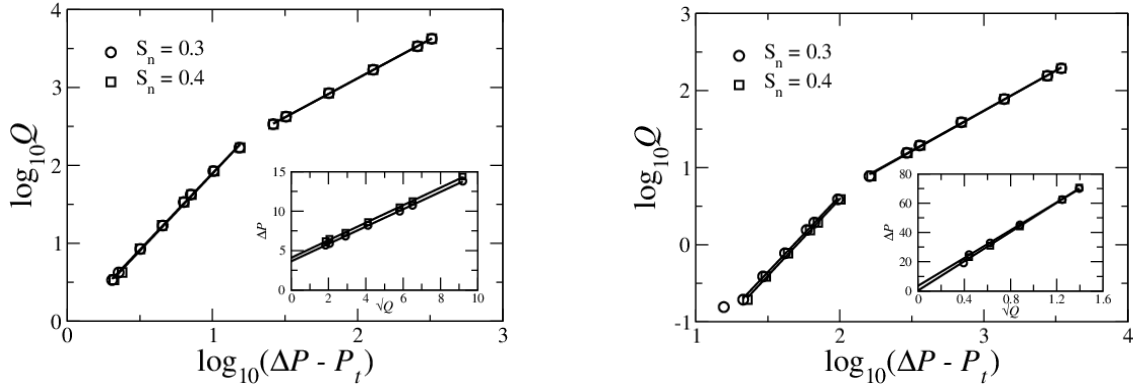


Fig. 12: Variation of the total volumetric flow rate Q (mm^3/s) with the overall pressure drop ΔP (kPa) in the steady state for square and Berea networks. In the inset, ΔP is plotted against \sqrt{Q} for the low Ca regime where the intercepts at the y -axis correspond to the values of threshold pressures (P_t). For 2D, we find $P_t = 3.65\text{kPa}$ and 4.09kPa for $S_n = 0.3$ and 0.4 respectively. For the Berea network in 3D, we find $P_t = 3.54\text{kPa}$ and 0.32kPa for $S_n = 0.3$ and 0.4 respectively. Using these values, we plot $\log_{10} Q$ versus $\log_{10}(\Delta P - P_t)$ which shows two distinct regimes at low and high pressures. For the linear regime, the slopes are obtained as 0.99 ± 0.01 and 1.00 ± 0.01 for 2D and 1.03 ± 0.01 and 1.04 ± 0.01 for 3D for the two saturations respectively. For the quadratic regime, the slopes are obtained as 1.96 ± 0.02 and 1.98 ± 0.03 for 2D and 1.98 ± 0.03 and 1.99 ± 0.04 for 3D.

rate Q in the steady state vary quadratically with the excess pressure drop. We can write as the following,

$$\begin{aligned} Q &= 0 & , & \quad P \leq P_t \\ &\sim (\Delta P - P_t)^2 & , & \quad P > P_t \end{aligned} \quad (13)$$

The quadratic regime corresponds to when the individual pores keep opening with the increasing pressure drop. Due to this, more and more flow paths appear in the system which makes the flow rate to increase faster than ΔP . When the capillary number is high enough, there is a transition from the quadratic regime and the flow rate becomes linear with the pressure drop. To verify whether our model can produce this cross-over, we performed steady-state simulations at constant flow rate Q . The results are presented in figure 12. The threshold pressures P_t are calculated by plotting ΔP versus \sqrt{Q} as shown in the insets. When the results follow equation 13, it will produce straight lines for the lower values of ΔP , where the intercepts of the straight lines at y -axis correspond to the values of P_t . Using these values of P_t , we plot Q versus $(\Delta P - P_t)$ in the log-log scale the disordered 2D network and the reconstructed 3D network. Results are shown in figure 12 which show two distinct regimes, a quadratic regime with slope ≈ 2 at the low pressure drops and a linear regime with slope ≈ 1 at higher pressure drops. A detailed numerical study on this non-linear effective rheological properties using the interface algorithms presented here can be found in [15], where the results are also compared with experiments.

5.2.2 Relation between seepage velocities

We will now measure the seepage velocities of the fluids in the steady state with this model and will verify the relations between them. When the system is driven under a constant pressure drop ΔP , a set of equations relating the wetting and non-wetting seepage velocities (v_w, v_n) to the total seepage velocity v and the fluid saturations can be derived using the Euler homogeneity property of the total flow rate Q in the steady state [23]. These relations necessitate a new velocity function, namely the co-moving velocity (v_m), which is a characteristic of the porous medium. The seepage velocities for the wetting and non-wetting fluids are defined as

$$v_w = \frac{Q_w}{A_w} \quad \text{and} \quad v_n = \frac{Q_n}{A_n} \quad (14)$$

respectively, where Q_w and Q_n are the volumetric flow rates of the two fluids in the direction of the applied pressure drop. Quantitatively, Q_w and Q_n are defined as the volume of the wetting and non-wetting fluids

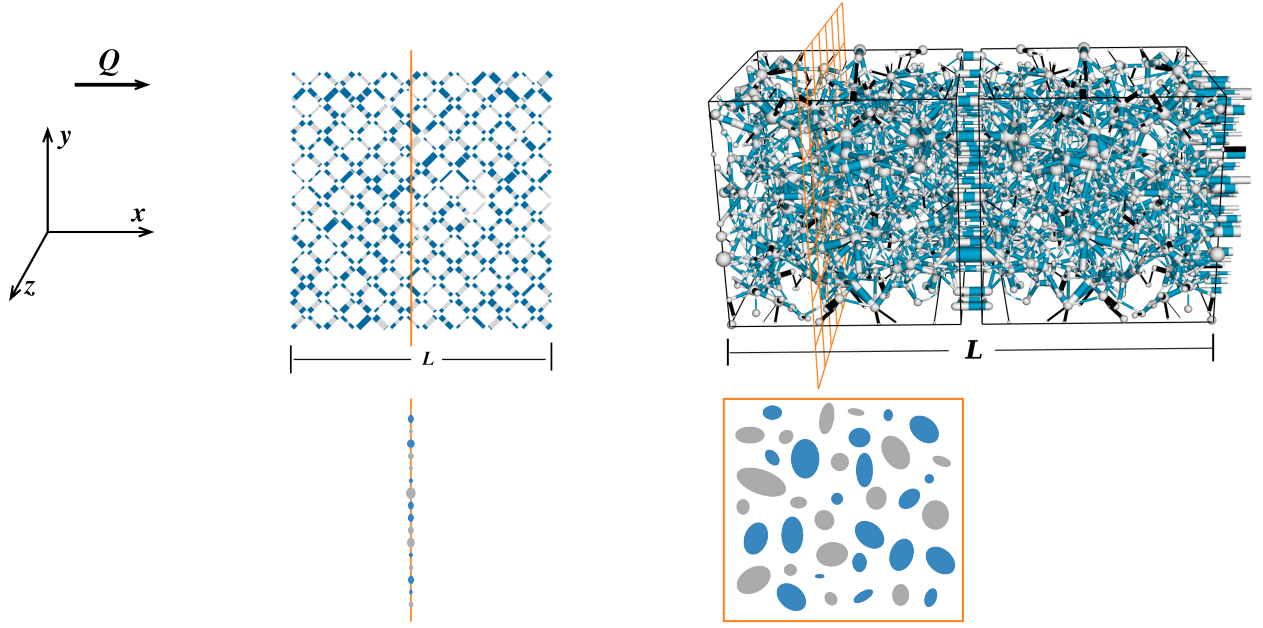


Fig. 13: Description of the system to measure the flow rates (Q , Q_w , Q_n), the pore areas (A , A_w , A_n) and the seepage velocities (v , v_w , v_n) for the 2D and 3D networks. The global pressure drop ΔP is applied in the x direction which is the direction of overall flow. A random cross section of the system normal to direction of overall flow is shown by the orange line for 2D and by the orange grid plane for 3D. The normal view of the cross sections are shown underneath where the gray and blue patches show the occupation by wetting and non-wetting fluids in the cross section. The total gray and blue areas correspond to the wetting and non-wetting pore areas respectively and the sum of them correspond to the total pore area along this cross section. The averages of these areas over all the possible cross sections lead to the measurement of A , A_w and A_n . In this figure, the gray a blue patches shown in the normal view of the cross sections do not reflect the actual occupations of the fluids in the above networks and are given as illustration purpose only.

that pass through any cross section of the system, perpendicular to the overall flow direction, per unit time. A_w and A_n are the wetting and non-wetting pore areas defined as the areas occupied by the wetting and non-wetting fluids along any orthogonal cross section through the system. This is illustrated in figure 13 where ΔP is applied in the positive x direction. The length of the systems in this direction is L . A cross section normal to the x direction is shown by an orange straight line for the 2D network and by an orange grid plane for the 3D network. Orthogonal views of these cross sections are shown underneath where the gray and blue patches show the pore areas occupied by the wetting and non-wetting fluids respectively. The sum of the areas of individual colors correspond to the wetting and non-wetting pore areas A_w and A_n along this cross section. For a homogeneous porous medium the average values of A_w and A_n remain same for any orthogonal cross section of the system in the steady state. Here we measure A_w and A_n by averaging the pore areas over all possible cross sections along x . The total pore area A related to all the fluids is therefore given by $A = A_w + A_n = \phi A_s$ where ϕ is the porosity and A_s is the average cross-sectional area of the total system including the pore space and the solid. With this, we can express the fluid saturations S_w and S_n in terms of the pore areas by $S_{w,n} = V_{w,n}/V_p = (A_{w,n}L)/(AL) = A_{w,n}/A$. The total flow rate Q of the two fluids is the sum of the wetting and non-wetting flow rates given by $Q = Q_w + Q_n = A_w v_w + A_n v_n$. Correspondingly, the total seepage velocity v associated with the total flow rate Q is defined by,

$$v = \frac{Q}{A} \quad (15)$$

and we can find,

$$v = S_w v_w + S_n v_n \quad (16)$$

by using the relations mentioned above.

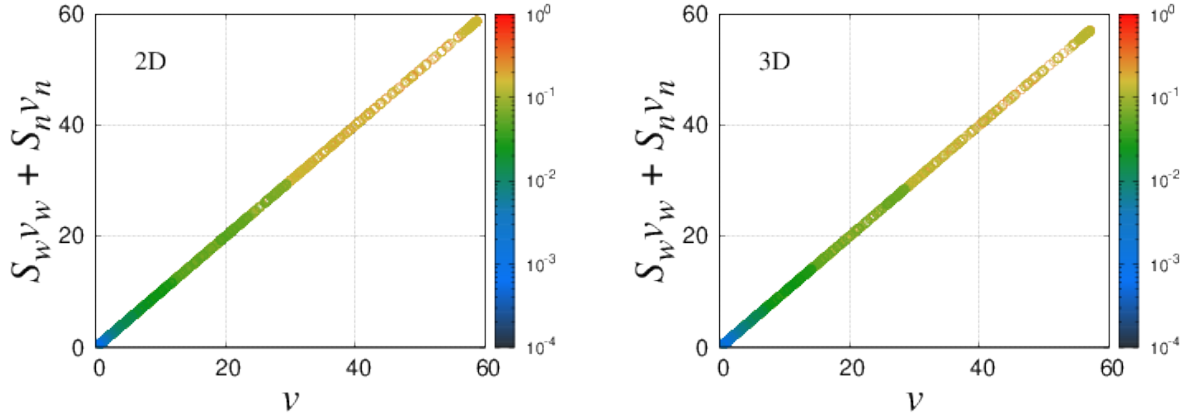


Fig. 14: Plot of $S_w v_w + S_n v_n$ against the total seepage velocity v for 2D and 3D. The flow rates and pore areas to calculate v_w , v_n and v are measured using the equations 17 and 18 for 2D and using 19 and 20 for 3D. The velocities are in the unit of mm/s. The colors represent the capillary numbers which are in the range of $0.0007 - 0.2985$ for 2D and $0.001 - 0.271$ for 3D. The measurements show the exact match of equation 16 for both 2D and 3D.

In our network simulations we have the information about the local flow rates q_i and the interface positions for each link i at any time step. However, calculating the average flow rates and the pore areas along any orthogonal cross section of the network from those quantities may not be straight forward, specially in case of an irregular network. For a regular network considered in 2D, all the links are of the same length $l_j = 1$ mm and they are oriented along the same angle (45°) with respect to the overall flow direction. The sum of the local flow rates through each row of links normal to the flow direction is therefore the same for any row and the flow rates can therefore be measured by summing over all the links of the network and then dividing by the number of rows. This given by,

$$Q = \frac{1}{N_L} \sum_j q_j, \quad Q_w = \frac{1}{N_L} \sum_j s_{w,j} q_j \quad \text{and} \quad Q_n = \frac{1}{N_L} \sum_j (1 - s_{w,j}) q_j \quad (17)$$

where N_L is the number of rows along L , i. e. 64 here. Similarly, we can calculate the cross-sectional areas as,

$$A = \frac{1}{N_L} \sum_j a_j, \quad A_w = \frac{1}{N_L} \sum_j s_{w,j} a_j \quad \text{and} \quad A_n = \frac{1}{N_L} \sum_j (1 - s_{w,j}) a_j \quad (18)$$

where a_j is the cross-sectional area of the link j , projected into the plane normal to the flow direction. The wetting saturations of the links $s_{w,j}$ are provided by the interface positions. Here the individual terms corresponding to the wetting and non-wetting phases are multiplied with the corresponding link saturations as the probability that a cross section through a link will pass through the wetting or non-wetting phase is proportional to the link saturation of that phase.

For an irregular network that is considered here in 3D, the links are of different lengths and oriented in different directions. In that case, measurement of the flow rates and the areas by summing over all the links and dividing by the number of rows using the equations 18 leads to wrong results. In this case, we measure these quantities in the following way. Let us consider an orthogonal cross-sectional plane at a random position through which we like to measure the flow rates (figure 13). The probability that any link j will pass through this plane will be proportional to $l_{x,j}/L$ where $l_{x,j}$ is the length of the link j in the x direction, the direction of the overall flow. After the link is selected, the probability that the plane will pass through the wetting fluid inside the link will be proportional to the local wetting saturation $s_{w,j}$ of the link. Considering these probabilistic terms, the total flow rates Q , Q_w and Q_n through a random orthogonal cross section can therefore be calculated from the

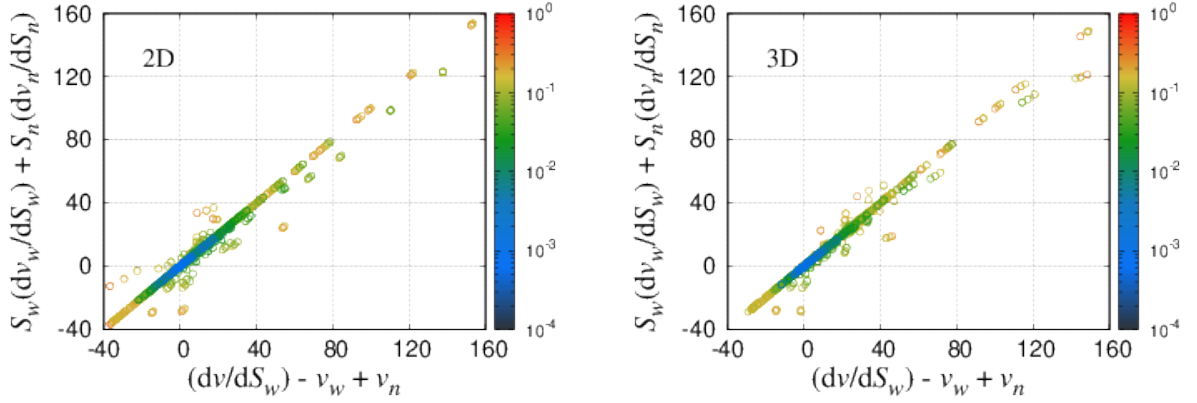


Fig. 15: Plot of the co-moving velocity v_m calculated using equation 26, $v_m = S_w(dv_w/dS_w) + S_n(dv_n/dS_n)$ versus the same using equation 25, $v_m = (dv/dS_w) - v_w + v_n$ for the square and Berea networks. The velocities are in the unit of mm/s. The data shows good a agreement with the equations 26 and 25 for the whole range of capillary numbers.

sum of the local flow rates over the links which pass through this cross section,

$$Q = \frac{1}{L} \sum_j l_{x,j} q_j, \quad Q_w = \frac{1}{L} \sum_j l_{x,j} s_{w,j} q_j \quad \text{and} \quad Q_n = \frac{1}{L} \sum_j l_{x,j} (1 - s_{w,j}) q_j \quad (19)$$

where L is the length of the network in the x direction. The areas can be measured in the similar way given by,

$$A = \frac{1}{L} \sum_j l_{x,j} a_j, \quad A_w = \frac{1}{L} \sum_j l_{x,j} s_{w,j} a_j \quad \text{and} \quad A_n = \frac{1}{L} \sum_j l_{x,j} (1 - s_{w,j}) a_j. \quad (20)$$

For the regular 2D network, $l_{x,j}$ are the same for all the links ($= l$) and we recover equations 17 and 18 by using $N_L = L/l$. After measuring the flow rates and the pore areas, the seepage velocities v , v_w and v_n are calculated using the equations 15 and 27. Results are averaged over time in the steady state.

The calculation of v , v_w and v_n from the measurements of the flow rates and the pore areas should satisfy equation 16. In figure 14, we plot $S_w v_w + S_n v_n$ against the total seepage velocity v where we used the equations 17 and 18 for 2D and the equations 19 and 20 for 3D. Figure 14 shows an exact match of equation 16 for the whole range of parameters.

The total flow rate Q in the steady state is a homogeneous function of order one of the pore areas A_w and A_n , that is, if we scale the three areas by $A \rightarrow \lambda A_w$, $A_n \rightarrow \lambda A_n$ and $A_s \rightarrow \lambda A_s$ by keeping the porosity ϕ constant, the volumetric flow rate Q scales as, $Q(\lambda A_w, \lambda A_n) = \lambda Q(A_w, A_n)$. This property of Q leads to a new set of equations between the seepage velocities. Complete derivations of the equations can be found in reference [23] and here we will present them in brief and will use them to validate our model. Taking the derivative of the homogeneity equation of Q with respect to λ and then setting $\lambda = 1$ we get,

$$v = S_w \left(\frac{\partial Q}{\partial A_w} \right)_{A_n} + S_n \left(\frac{\partial Q}{\partial A_n} \right)_{A_w}. \quad (21)$$

These two partial derivatives in the above equation have the units of velocity and correspondingly they define two thermodynamic velocities \hat{v}_w and \hat{v}_n given by,

$$\hat{v}_w = \left(\frac{\partial Q}{\partial A_w} \right)_{A_n} \quad \text{and} \quad \hat{v}_n = \left(\frac{\partial Q}{\partial A_n} \right)_{A_w}. \quad (22)$$

With these definitions equation 21 becomes,

$$v = S_w \hat{v}_w + S_n \hat{v}_n, \quad (23)$$

which has the similar form of equation 16. However, this does *not* imply that the thermodynamic velocities \hat{v}_w and \hat{v}_n are the same as the seepage velocities v_w and v_n that we measure. These two types of velocities can be related by a new velocity function is v_m given by,

$$\hat{v}_w = v_w + S_n v_m \text{ and } \hat{v}_n = v_n - S_w v_m \quad (24)$$

which fulfill both the equations 16 and 23. This velocity function v_m is a function of the saturation S_w and called as the co-moving velocity, which is a property of the pore-network. With this definition of v_m , we can derive two equations that are related to the variation of saturation,

$$\frac{dv}{dS_w} = v_w - v_n + v_m \quad (25)$$

and

$$S_w \frac{dv_w}{dS_w} + (1 - S_w) \frac{dv_n}{dS_n} = v_m. \quad (26)$$

In order to verify whether our pore-network model with the set of interface algorithms described here do satisfy these equations, we perform a large number of simulations with a wide range of parameters for the 2D square network and the 3D Berea network. Five viscosity ratios, $M = 0.5, 1, 2, 5$ and 10 are considered where the wetting viscosity is chosen as $\mu_w = 0.1$ Pa s. The non-wetting viscosity μ_n is then chosen accordingly in order to set the value of M . For each value of M , three different values of the surface tension, $\gamma = 0.02, 0.03$ and 0.04 N/m, are considered. For each set of M and γ , we considered a set of pressure drops $|\Delta P/L| = 0.16, 0.20, 0.40, 0.80, 1.0$ and 2.0 MPa/m for 2D and $10, 20, 40, 80$ and 160 MPa/m for 3D. These values of pressure drops are chosen in order to get capillary numbers Ca in a range around 10^{-3} to 10^{-1} . Specifically, we find Ca in the range of $0.0007 - 0.2985$ for 2D and $0.001 - 0.271$ for 3D. For any set of parameters, saturations are varied in the range of 0 to 1 in the steps of 0.05 which correspond to 21 saturation values. This led to a total of 1890 independent simulations for 2D and 1575 simulations for 3D in steady state.

The seepage velocities are measured for all the simulations and the derivatives with respect to the saturations are measured with central difference technique. We calculate the values of $v_m = (dv/dS_w) - v_w + v_n$ (equation 25) and $v_m = S_w(dv_w/dS_w) + S_n(dv_n/dS_n)$ (equation 26) and plot in figure 15. The results show good agreement with the equation 25 and 26 for both square and Berea networks for the whole range of the capillary numbers as indicated by the color scale. The few data points that are outside the straight line mostly correspond to the simulations near $S_w = 0$ or 1 where the system undergoes from two-phase to single phase regime that creates a jump in the derivatives.

Equations 16 and 26 transforms the wetting and non-wetting velocities (v_w, v_n) to (v, v_m) while varying the saturation. By inverting the velocity transformation, it is possible to find equations to transform the total velocity and the co-moving velocity (v, v_m) to (v_w, v_n) , which are given by,

$$v_w = v + S_n \left(\frac{dv}{dS_w} - v_m \right) \text{ and } v_n = v - S_w \left(\frac{dv}{dS_w} - v_m \right). \quad (27)$$

With these equations we can verify the measured values of wetting and non-wetting seepage velocities v_w and v_n against the ones calculated from these equation. In figure 16, we plot $v + S_n(dv/dS_w - v_m)$ and $v - S_w(dv/dS_w - v_m)$ against the measured value of v_w and v_n respectively. While calculating v_w and v_m using above equations, we used the values of v_m that are obtained from equation 26. For the whole range of the capillary numbers, good match with equations 27 can be observed for both the square and the Berea networks.

Finally, we plot the co-moving velocity v_m as a function of both S_w and dv/dS_w in figure 17. The co-moving velocity is a property of the porous material and a function of the saturation S_w , total seepage velocity v and the variation of v while changing the saturation. It is not enough to specify only the S_w and v to determine v_m , as dv/dS_w depends on how the external parameters are controlled while varying the S_w . Here v_m was calculated using equation 25 in figure 17. The data for v_m roughly shows a planer form given by,

$$v_m = a S_w + b \frac{dv}{dS_w} + c. \quad (28)$$

By fitting all the data points for the whole set of simulations, we find $a = -6.36 \pm 0.25$, $b = 0.94 \pm 0.01$ and $c = 5.00 \pm 0.13$ for the square network and $a = -12.94 \pm 0.62$, $b = 0.88 \pm 0.01$ and $c = 10.10 \pm 0.32$ for the Berea

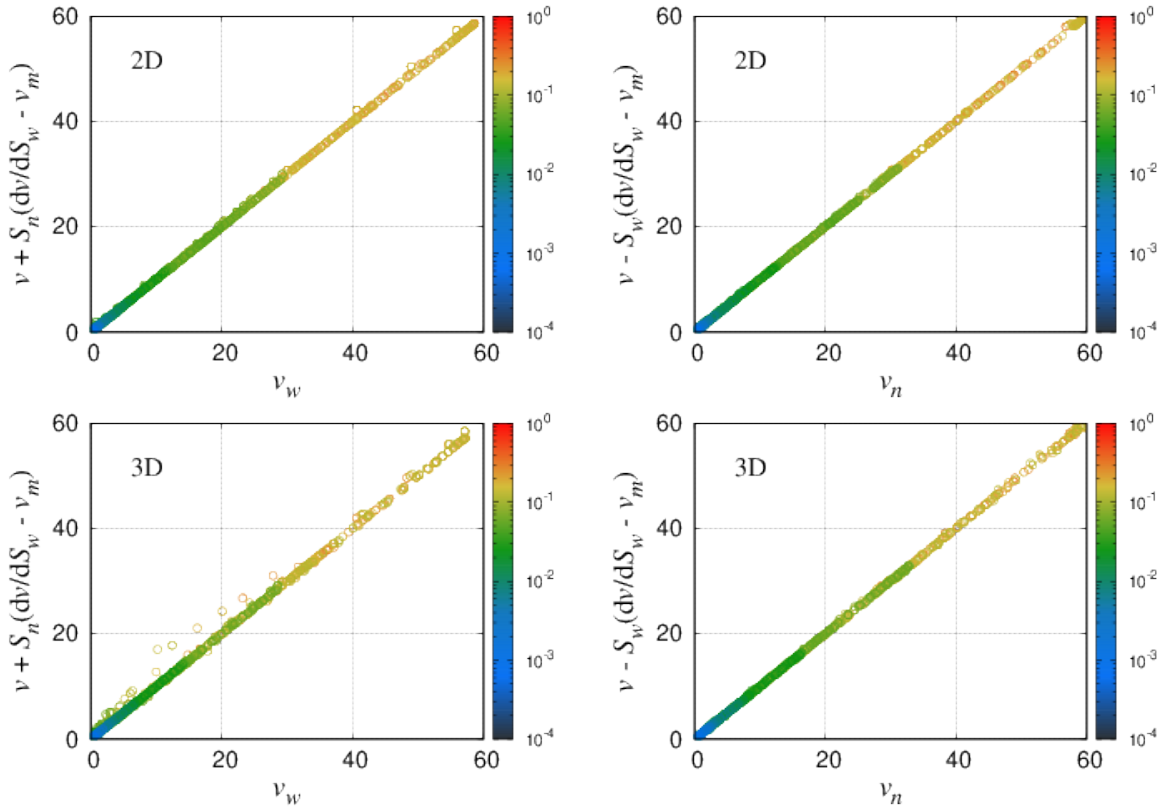


Fig. 16: Plot of the wetting and non-wetting seepage velocities (mm/sec) calculated using equations 27 against the measured values of v_w and v_n for the square (top row) and Berea (bottom row) network. The derivatives are calculated using the central difference techniques. The color scale shows the capillary numbers.

network. The planes using these parameters are shown in the respective figures with grid lines. Interestingly, the values of b are close to 1 which leads the data points to fall around the $y = x$ straight line while plotting v_m against dv/dS_w as shown the figure 17.

6 Summary

We presented a detailed description of a set of algorithms for transporting fluids in a dynamic pore-network model of two-phase flow in porous media. The displacements of the fluids in this model are monitored by updating the positions of all the interfaces with time. The basic concept of the algorithms are simple, at every time step all the fluids arriving at a node from the incoming links are displaced to all the outgoing links, and the volumes of the fluids are distributed according to the ratio of the fluxes of the outgoing links. Our aim in this article is to present these algorithms with all the technical details so that it is possible for the reader to reproduce this model. We have illustrated that this pore-network model and the interface algorithms are applicable for both the regular and irregular network topologies as well as for both two and three dimensional pore networks. Moreover, by reproducing some of the fundamental results of two-phase flow, we have also shown that the model can be used to simulate both the transient and steady-state flow. We have shown different drainage flow patterns that can be generated with this model when a fluid displaces the other in a porous medium. In steady state, the model successfully reproduces the linear to non-linear transition in the effective rheological properties as well as the relations between the seepage velocities.

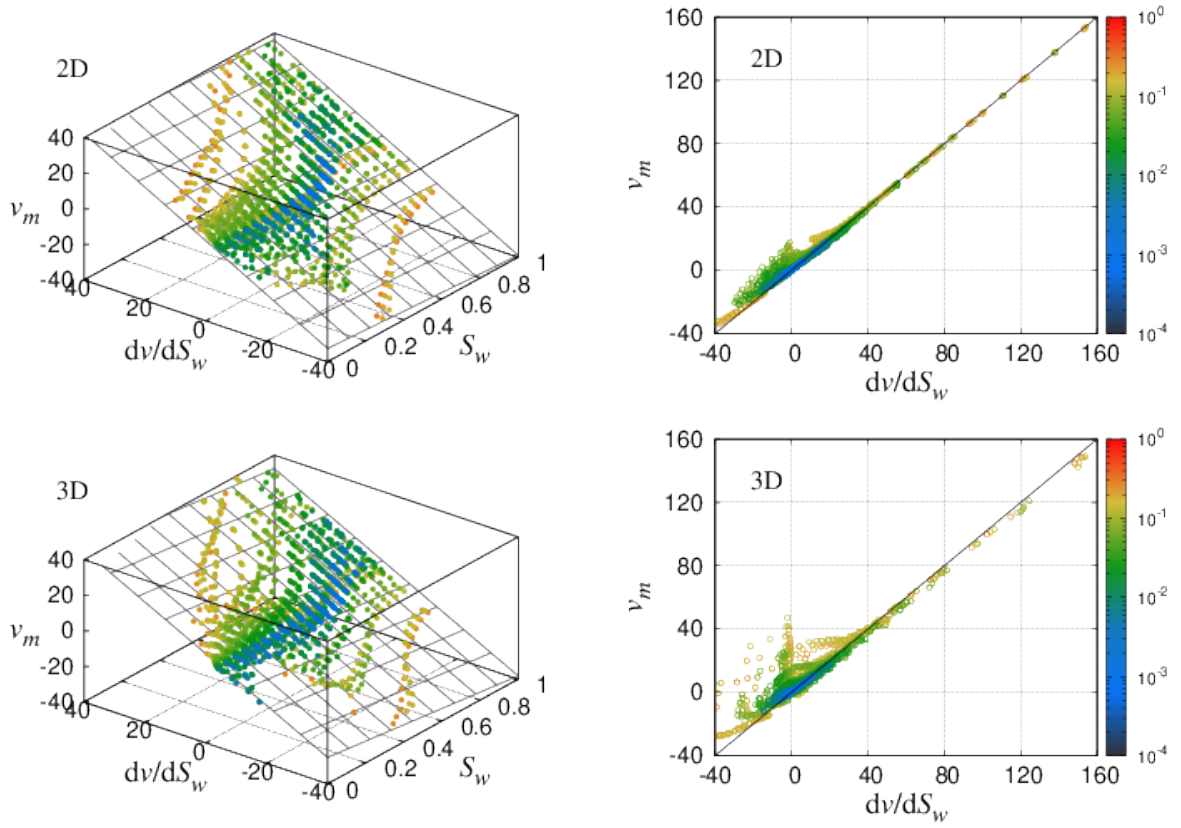


Fig. 17: Plot of the co-moving velocity v_m as a function of S_w and dv/dS_w for the square (2D) and Berea (3D) networks are shown in the left. The data shows a rough planner behavior. The projection of the plots on the $y - z$ plane is shown in the right, where the values of v_m roughly follow the $y = z$ straight line.

In a recent paper by Zhao et al. [4] ten different groups with different approaches to modeling two-phase flow in porous media were invited to reproduce fluid injection in a circular Hele-Shaw cell at different capillary numbers and wetting properties, ranging from drainage to strong imbibition, i.e., imbibition where film flow dominates the process. The conclusion of that work was, whereas all the different approaches were able to reproduce the drainage processes well, none succeeded in reproducing strong imbibition. Film flow is an important mechanism during imbibition and in a first attempt, we expanded our model in [47] to include films. However, this work has so far not been followed up by us.

The time integration procedure is time consuming. In [49], Savani et al. proposed a Monte Carlo algorithm to replace the time integration. This approach promises a large increase in efficiency of the model. However, the method needs to be tested at low capillary numbers. Moreover, it has so far only been implemented for regular lattices and needs to be generalized to realistic pore networks.

Acknowledgments

We thank our co-workers, past and present, who have been involved in developing this model through its various stages, Eyvind Aker, G. George Batrouni, M. Grøva, Henning A. Knudsen, Knut Jørgen Måløy, Pål Eric Øren, Thomas Ramstad, Subhadeep Roy, Isha Savani and Glen Tørå. This work was partly supported by the Research Council of Norway through its Centres of Excellence funding scheme, project number 262644. SS was supported by the National Natural Science Foundation of China under grant number 11750110430.

References

1. F. A. L. Dullien, *Porous Media: Fluid Transport and Pore Structure* (Academic Press, San Diego, 1992).
2. J. Bear, *Dynamics of fluids in porous media*, Mineola, NY: Dover (1988).
3. Løvoll G, Méheust Y, Toussaint R, Schmittbuhl J, Måløy KJ. Growth activity during fingering in a porous Hele-Shaw cell. *Phys Rev E*. (2004) **70**:026301. doi: 10.1103/PhysRevE.70.026301
4. B. Zhao, C. W. MacMinn, B. K. Primkulov, Y. Chen, A. J. Valocchi, J. Zhao, Q. Kang, K. Bruning, J. E. McClure, C. T. Miller, A. Fakhari, D. Bolster, T. Hiller, M. Brinkmann, L. Cueto-Felgueroso, D. A. Cogswell, R. Verma, M. Prodanovic, J. Maes, S. Geiger, M. Vassvik, A. Hansen, E. Segre, R. Holtzman, Z. Yang, C. Yuan, B. Chareyre and R. Juanes, Comprehensive comparison of pore-scale models for multiphase flow in porous media, *Proc. Natl. Acad. Sci. U.S.A.* **116**, 13799 (2019). doi: 10.1073/pnas.1901619116
5. R. Lenormand, E. Touboul, C. Zarcone, Numerical models and experiments on immiscible displacements in porous media. *J Fluid Mech.* (1988) **189**:165. doi: 10.1017/S0022112088000953
6. K. J. Måløy, J. Feder and T. Jøssang, Viscous fingering fractals in porous media, *Phys. Rev. Lett.* **55**, 2688 (1985). doi: 10.1103/PhysRevLett.55.2688
7. R. Lenormand and C. Zarcone, Invasion percolation in an etched network: measurement of a fractal dimension, *Phys. Rev. Lett.* **54**, 2226 (1985). doi: 10.1103/PhysRevLett.54.2226
8. D. Wilkinson and J. F. Willemsen, Invasion percolation: a new form of percolation theory, *J. Phys. A: Math. Gen.* **16**, 3365 (1983). doi: 10.1088/0305-4470/16/14/028
9. T. A. Witten Jr. and L. M. Sander, Diffusion-limited aggregation, a kinetic critical phenomenon, *Phys. Rev. E* **47**, 1400 (1981). doi: 10.1103/PhysRevLett.47.1400
10. L. Paterson, Diffusion-Limited Aggregation and Two-Fluid Displacements in Porous Media, *Phys. Rev. Lett.* **52**, 1621 (1984). doi: 10.1103/PhysRevLett.52.1621
11. K. T. Tallakstad, H. A. Knudsen, T. Ramstad, G. Løvoll, K. J. Måløy, R. Toussaint and E. G. Flekkøy, Steady-state two-phase flow in porous media: statistics and transport properties, *Phys. Rev. Lett.* **102**, 074502 (2009). doi: 10.1103/PhysRevLett.102.074502
12. K. T. Tallakstad, G. Løvoll, H. A. Knudsen, T. Ramstad, E. G. Flekkøy and K. J. Måløy, Steady-state, simultaneous two-phase flow in porous media: An experimental study, *Phys. Rev. E* **80**, 036308 (2009). doi: 10.1103/PhysRevE.80.036308
13. E. M. Rassi, S. L. Codd SL and J. D. Seymour, Nuclear magnetic resonance characterization of the stationary dynamics of partially saturated media during steady-state infiltration flow, *New J. Phys* **13**, 015007 (2011). doi: 10.1088/1367-2630/13/1/015007
14. S. Sinha and A. Hansen, Effective rheology of immiscible two-phase flow in porous media, *Europhys. Lett.* **99**, 44004 (2012). doi: 10.1209/0295-5075/99/44004
15. S. Sinha, A. T. Bender, M. Danczyk, K. Keepseagle, C. A. Prather, J. M. Bray, L. W. Thrane, J. D. Seymour, S. L. Codd and A. Hansen, Effective rheology of two-phase flow in three-dimensional porous media: Experiment and simulation, *Transp. Porous Med.* **119**, 77 (2017). doi: 10.1007/s11242-017-0874-4
16. P. G. Saffman and G. I. Taylor, The penetration of a fluid into a porous medium or Hele-Shaw cell containing a more viscous liquid, *Proc. Royal Soc. A: Math. Phys. Eng. Sc.* **245**, 312 (1958). doi: 10.1098/rspa.1958.0085
17. J. D. Chen and D. Wilkinson, Pore-scale viscous fingering in porous media, *Phys. Rev. Lett.* **55**, 1892 (1985). doi: 10.1103/PhysRevLett.55.1892
18. D. Bensimon, L. P. Kadanoff, S. Liang, B. I. Shraiman and C. Tang, Viscous flows in two dimensions, *Rev. Mod. Phys.* **58**, 977 (1986). doi: 10.1103/RevModPhys.58.977
19. J. Koplik and T. J. Lasseter, Two-Phase Flow in Random Network Models of Porous Media, *Soc. Petro. Eng. J.* **25**, 89 (1985). doi: 10.2118/11014-PA
20. S. M. Hassanizadeh and W. G. Gray, Toward an improved description of the physics of two-phase flow, *Adv. Water Res.* **16**, 53 (1993). doi: 10.1016/0309-1708(93)90029-F
21. R. Hilfer, Macroscopic equations of motion for two-phase flow in porous media, *Phys. Rev. E* **58**, 2090 (1998). doi: 10.1103/PhysRevE.58.2090
22. W. G. Gray and C. T. Miller, *Introduction to the Thermodynamically Constrained Averaging Theory for Porous Medium Systems* (Springer, Berlin, 2014).
23. A. Hansen, S. Sinha, D. Bedeaux, S. Kjelstrup, M. A. Gjennestad and M. Vassvik, Relations between seepage velocities in immiscible, incompressible two-phase flow in porous media, *Transp. Porous Med.* **125**,

- 565 (2018). doi: 10.1007/s11242-018-1139-6
24. A. Q. Raeini, M. J. Blunt, and B. Bijeljic, Modelling two-phase flow in porous media at the pore scale using the volume-of-fluid method, *J. Comput. Phys.* **231** 5653 (2012). doi: 10.1016/j.jcp.2012.04.011
 25. E. Jettestuen, J. O. Helland and M. Prodanovic, A level set method for simulating capillary-controlled displacements at the pore scale with nonzero contact angles, *Water Resour. Res.* **49**, 4645 (2013). doi: 10.1002/wrcr.20334
 26. M. A. Gjennestad and S. T. Munkejord, Modelling of heat transport in two-phase flow and of mass transfer between phases using the level-set method, *Energy Proc.* **64** 53 (2015). doi: 10.1016/j.egypro.2015.01.008
 27. A. K. Gunstensen, D. H. Rothman, S. Zaleski and G. Zanetti, Lattice Boltzmann model of immiscible fluids, *Phys. Rev. A.* **43** 4320 (1991). doi: 10.1103/PhysRevA.43.4320
 28. T. Ramstad, P. E. Øren and S. Bakke, Simulation of two-phase flow in reservoir rocks using a lattice Boltzmann method, *SPE J.* **15**, 917 (2010). doi: 10.2118/124617-PA
 29. O. Aursjø, G. Løvoll, H. A. Knudsen, E. G. Flekkøy and K. J. Måløy, A direct comparison between a slow pore scale drainage experiment and a 2D lattice Boltzmann simulation, *Transp. Porous Med.* **86**, 125 (2011). doi: 10.1007/s11242-010-9611-y
 30. V. Joekar-Niasar and S. M. Hassanizadeh, Analysis of fundamentals of two-phase flow in porous media using dynamic pore-network models: a review, *Crit. Rev. Environ. Sc. Tech.* **42**, 1895 (2012). doi: 10.1080/10643389.2011.574101
 31. M. J. Blunt, Flow in porous media – pore-network models and multiphase flow, *Current Opinion in Colloid & Interface Science* **6**, 197 (2001). doi: 10.1016/S1359-0294(01)00084-X
 32. R. Chandler, J. Koplik, K. Lerman and J. F. Willemsen, Capillary displacement and percolation in porous media, *J. Fluid Mech.* **119**, 249 (1982). doi: 10.1017/S0022112082001335
 33. M. J. Blunt, Physically-based network modeling of multiphase flow in intermediate-wet porous media, *J. Petro. Sc. Eng.* **20**, 117 (1999). doi: 10.1016/S0920-4105(98)00010-2
 34. M. Cieplak and M. O. Robbins, Dynamical Transition in Quasistatic Fluid Invasion in Porous Media, *Phys. Rev. Lett.* **60**, 2042 (1988). doi: 10.1103/PhysRevLett.60.2042
 35. M. Cieplak and M. O. Robbins, Influence of contact angle on quasistatic fluid invasion of porous media, *Phys. Rev. B* **41**, 115508 (1990). doi: 10.1103/PhysRevB.41.11508
 36. P.-E. Øren, S. Bakke and O. J. Arntzen, Extending Predictive Capabilities to Network Models, *SPE Journal* **3**, 324 (1998). doi: 10.2118/52052-PA
 37. M. J. Blunt, M. D. Jackson, M. Piri and P. H. Valvatne, Detailed physics, predictive capabilities and macroscopic consequences for pore-network models of multiphase flow, *Adv. Water Resources* **25**, 1069 (2002). doi: 10.1016/S0309-1708(02)00049-0
 38. B. K. Primkulov, S. Talman, K. Khaleghi, A. R. Shokri, R. Chalaturnyk, B. Zhao, C. W. MacMinn and R. Juanes, Quasistatic fluid-fluid displacement in porous media: Invasion-percolation through a wetting transition, *Phys. Rev. Fluids* **3**, 104001 (2018). doi: 10.1103/PhysRevFluids.3.104001
 39. V. Joekar-Niasar, S. M. Hassanizadeh and H. Dahle, Non-equilibrium effects in capillarity and interfacial area in two-phase flow: dynamic pore-network modelling, *J. Fluid Mech.* **655**, 38 (2010). doi: 10.1017/S0022112010000704
 40. P. S. Hammond and E. Unsal, A dynamic pore network model for oil displacement by wettability-altering surfactant solution, *Trans. Porous Media* **92**, 789 (2012). doi: 10.1007/s11242-011-9933-4
 41. E. Aker, K. J. Måløy, A. Hansen and G. G. Batrouni, A two-dimensional network simulator for two-phase flow in porous media, *Transp. Porous Med.* **32**, 163 (1998). doi: 10.1023/A:1006510106194
 42. W. B. Haines, Studies in the physical properties of soil. v. the hysteresis effect in capillary properties, and the modes of moisture distribution associated therewith, *J. Agric. Sci.* **20**, 97 (1930). doi: 10.1017/S002185960008864X
 43. S. Berg, H. Ott, S. A. Klapp, A. Schwing, R. Neiteler, N. Brussee N, et al, Real-time 3D imaging of Haines jumps in porous media flow, *Proc. Natl. Acad. Sci. USA* **110**, 3755 (2013). doi: 10.1073/pnas.1221373110
 44. R. T. Armstrong and S. Berg, Interfacial velocities and capillary pressure gradients during haines jumps, *Phys. Rev. E* **88**, 043010 (2013). doi: 10.1103/PhysRevE.88.043010
 45. K. J. Måløy, L. Furuberg, J. Feder and T. Jøssang, Dynamics of slow drainage in porous media, *Phys. Rev. Lett.* **68**, 2161 (1992). doi: 10.1103/PhysRevLett.68.2161

46. H. A. Knudsen, E. Aker and A. Hansen, Bulk Flow Regimes and Fractional Flow in 2D Porous Media by Numerical Simulations, *Transp. Porous Med.* (2002) **47**:99. doi: 10.1023/A:1015039503551
47. G. Tørå, P. E. Øren and A. Hansen, A dynamic network model for two-phase flow in porous media, *Transp. Porous Med.* (2012) **92**:145. doi: 10.1007/s11242-011-9895-6
48. M. A. Gjennestad, M. Vassvik, S. Kjelstrup and A. Hansen, Stable and Efficient Time Integration of a Dynamic Pore Network Model for Two-Phase Flow in Porous Media, *Front. Phys.* **6**, 56 (2018).x doi: 10.3389/fphy.2018.00056
49. I. Savani, S. Sinha, A. Hansen, D. Bedeaux, S. Kjelstrup and M. Vassvik, A Monte Carlo algorithm for immiscible two-phase flow in porous media, *Transp. Porous Med.* **116**, 869 (2016). doi: 10.1007/s11242-016-0804-x
50. S. Sinha, M. Grøva, T. B. Ødegåden, E. Skjetne and A. Hansen, Local wettability reversal during steady-state two-phase flow in porous media, *Phys. Rev. E* **84**, 037303 (2011). doi: 10.1103/PhysRevE.84.037303
51. V. Flovik, S. Sinha and A. Hansen, Dynamic wettability alteration in immiscible two-phase flow in porous media: effect on transport properties and critical slowing down, *Front. Phys.* **3**, 86 (2015). doi: 10.3389/fphy.2015.00086
52. H. J. Vogel and K. Roth, Quantitative morphology and network representation of soil pore structure, *Adv. Water Res.* **24**, 233 (2001). doi: 10.1016/S0309-1708(00)00055-5
53. M. Erpelding, S. Sinha, K. T. Tallakstad, A. Hansen, E. G. Flekkøy and K. J. Måløy, History independence of steady state in simultaneous two-phase flow through two-dimensional porous media, *Phys. Rev. E* **88**, 053004 (2013). doi: 10.1103/PhysRevE.88.053004
54. T. Ramstad, A. Hansen and P. E. Øren, Flux-dependent percolation transition in immiscible two-phase flow in porous media, *Phys. Rev. E* **79**, 036310 (2009). doi: 10.1103/PhysRevE.79.036310
55. <https://www.imperial.ac.uk/earth-science/research/research-groups/perm/research/pore-scale-modelling/micro-ct-images-and-networks/>
56. H. Okabe and M. J. Blunt, Pore space reconstruction using multiple-point statistics, *J. Pet. Sci. Eng.* **46**, 121 (2005). doi: 10.1016/j.petrol.2004.08.002
57. P.-E. Øren and S. Bakke, Process based reconstruction of sandstones and prediction of transport properties, *Transp. Porous Med.* **46**, 311 (2002). doi: 10.1023/A:1015031122338
58. P.-E. Øren and S. Bakke, Reconstruction of berea sandstone and pore-scale modeling of wettability effects, *J. Pet. Sci. Eng.* **39**, 177 (2003). doi: 10.1016/S0920-4105(03)00062-7
59. H. Dong, Micro-CT Imaging and Pore Network Extraction, Ph.D. Thesis, Imperial College London (2007). <http://www3.imperial.ac.uk/pls/portallive/docs/1/43735696.PDF>
60. H. Dong and M. J. Blunt, Pore-network extraction from micro-computerized-tomography images, *Phys. Rev. E* **80**, 036307 (2009). doi: 10.1103/PhysRevE.80.036307
61. S. Sinha, A. Hansen, D. Bedeaux and S. Kjelstrup, Effective rheology of bubbles moving in a capillary tube, *Phys. Rev. E* **87**, 025001 (2013). doi: 10.1103/PhysRevE.87.025001
62. E. W. Washburn, The dynamics of capillary flow, *Phys. Rev.* **17**, 273 (1921). doi: 10.1103/PhysRev.17.273
63. G. Mason and N. R. Morrow, Capillary behavior of a perfectly wetting liquid in irregular triangular tubes, *J. Colloid Interface Sci.* **141**, 262 (1991). doi: 10.1016/0021-9797(91)90321-X
64. W. E. Langlois, *Slow Viscous Flow* (The Macmillan Company, New York, 1964).
65. P. Jia, M. Dong, L. Dai and J. Yao, Slow viscous flow through arbitrary triangular tubes and its application in modelling porous media flows, *Transp. Porous Med.* **74**, 153 (2008). doi: 10.1007/s11242-007-9187-3
66. G. G. Batrouni and A. Hansen, Fourier acceleration of iterative processes in disordered systems, *J. Stat. Phys.* **52**, 747 (1988). doi: 10.1007/BF01 019728
67. W. H. Press, S. A. Teukolsky, W. T. Vetterling and B. P. Flannery, *Numerical Recipes in C (2nd Ed.): The Art of Scientific Computing* (Cambridge University Press, New York, NY, USA, 1992).
68. S. Sinha, M. A. Gjennestad, M. Vassvik, M. Winkler, A. Hansen and E. G. Flekkøy, Rheology of High-Capillary Number Two-Phase Flow in Porous Media, *Front. Phys.* **7**, 65 (2019). doi: 10.3389/fphy.2019.00065
69. P. Garstecki, M. J. Fuerstman, H. A. Stonec and G. M. Whitesides, Formation of droplets and bubbles in a microfluidic T-junction – scaling and mechanism of break-up, *Lab Chip.* **6**, 437 (2006). doi: 10.1039/b510841a
70. S. Roy, A. Hansen and S. Sinha, Effective rheology of two-phase flow in a capillary fiber bundle model, *Front. Phys.* **7**, 92 (2019). doi: 10.3389/fphy.2019.00092